

USING LARGE-EDDY SIMULATIONS TO ANALYZE
MICROPHYSICAL BEHAVIOR IN MIDDLELEVEL, MIXED-PHASE
CLOUDS

by

Adam J. Smith

A Thesis Submitted in
Partial Fulfillment of the
Requirements for the Degree of

MASTER OF SCIENCE

in

MATHEMATICS

at

The University of Wisconsin–Milwaukee

December 2007

USING LARGE-EDDY SIMULATIONS TO ANALYZE
MICROPHYSICAL BEHAVIOR IN MIDDLELEVEL, MIXED-PHASE
CLOUDS

by

Adam J. Smith

A Thesis Submitted in
Partial Fulfillment of the
Requirements for the Degree of

MASTER OF SCIENCE

in

MATHEMATICS

at

The University of Wisconsin–Milwaukee

December 2007

Major Professor

Date

Graduate School Approval

Date

ABSTRACT

USING LARGE-EDDY SIMULATIONS TO ANALYZE MICROPHYSICAL BEHAVIOR IN MIDDLELEVEL, MIXED-PHASE CLOUDS

by

Adam J. Smith

The University of Wisconsin–Milwaukee, 2007
Under the Supervision of Professor Vincent E. Larson

This study examines the microphysical habits of three mid-level, mixed-phase cloud systems. Each cloud was sampled by aircraft, and three-dimensional large-eddy simulations are used to reproduce the conditions of the cloud systems. The simulations include a single-moment bulk method for calculating ice microphysics, allowing for a detailed analysis of the processes affecting the mixing ratios of cloud water and snow. Budget equations of liquid water and snow are presented, detailing the contributions of each major model process. The liquid water budget equation shows that depositional growth of snow provides the strongest microphysical contribution to cloud water depletion. Similarly, the snow budget equation indicates depositional growth produces the largest increase in snow mixing ratio within cloud, while sedimentation of snow acts to counter the growth by forcing snow to fall out of cloud. We also create a series of analytic equations based on the bulk microphysics scheme. These equations provide a simple method of predicting snow properties at the base of a mixed-phase layer without requiring a large amount of in-cloud information. A sensitivity study shows that the predictive equations provide a reasonable estimate of snow properties.

Major Professor

Date

© Copyright by Adam J. Smith, 2007
All Rights Reserved

TABLE OF CONTENTS

1	Introduction	1
2	Model description	4
2.1	A single-moment microphysical scheme	5
3	The Cloud Cases	7
3.1	The Nov.11 cloud	7
3.2	The Oct.14 cloud	8
3.3	The Nov.02 cloud	10
3.4	Comparisons of the simulated profiles versus aircraft data	11
3.5	Time evolution of liquid and snow	14
4	Budgets showing primary effects on cloud water and snow mixing ratio	28
4.1	A budget for the time evolution of cloud water mixing ratio	28
4.2	A budget for the time evolution of snow mixing ratio	31
5	The development of analytic formulas for predicting snow mixing ratio and snow precipitation flux	39
6	Verification of the snow mixing ratio and snow precipitation flux formulas	46
7	Conclusions	51
	Bibliography	53

LIST OF FIGURES

3.1	A comparison of simulated liquid water mixing ratio (r_c) in the Nov.11 control simulation versus the available aircraft sounding. A solid line denotes the simulated profile, while symbols represent the observed aircraft conditions. The simulated profile is obtained at $t = 61$ min, immediately after the model spinup period is completed.	15
3.2	Same as figure 3.1, except for the Oct.14 control simulation. Here, three different symbols are used to denote data from all three available aircraft soundings.	15
3.3	Same as figure 3.2, except for the Nov.02 control simulation.	16
3.4	A comparison of simulated water vapor mixing ratio (r_v) in the Nov.11 control simulation versus the available aircraft sounding. Dots represent the simulated profile, while a thin line indicates the observed aircraft profile. The simulated profile is obtained at $t = 61$ min, immediately after the model spinup period is completed.	16
3.5	Same as figure 3.4, except for the Oct.14 control simulation. A supplemental rawinsonde sounding (dashed line) is included to verify that the simulated above- and below-cloud profile matches environmental conditions where the aircraft sampling did not occur. The simulated saturation mixing ratio at $t = 61$ min is also provided (stars), to demonstrate the saturation conditions within our simulation.	17
3.6	Same as figure 3.5, except for the Nov.02 control simulation.	17
3.7	A comparison of simulated potential temperature (θ) in the Nov.11 control simulation versus the available aircraft sounding. Dots represent the simulated profile, while a thin line indicates the observed aircraft profile. The simulated profile is obtained at $t = 61$ min, immediately after the model spinup period is completed.	18
3.8	Same as figure 3.7, except for the Oct.14 control simulation. A supplemental rawinsonde sounding (dashed line) is included to verify that the simulated above- and below-cloud profile matches environmental conditions where the aircraft sampling did not occur.	18
3.9	Same as figure 3.7, except for the Nov.02 control simulation.	19
3.10	A comparison of simulated snow mixing ratio (r_s) in the Nov.11 control simulation versus the available aircraft sounding. A solid line denotes the simulated profile, while symbols represent the observed aircraft conditions. The simulated profile is obtained at $t = 90$ min, to account for a spinup period for the microphysics scheme.	20
3.11	Same as figure 3.10, except for the Oct.14 control simulation. Here, three different symbols are used to denote data from all three available aircraft soundings.	21
3.12	Same as figure 3.11, except for the Nov.02 control simulation.	21

3.13	A contour plot showing the evolution of liquid water mixing ratio, r_c , for the Nov.11 control simulation.	22
3.14	A contour plot showing the evolution of snow mixing ratio, r_S , for the Nov.11 control simulation.	23
3.15	Same as figure 3.13, but for the Oct.14 control simulation.	24
3.16	Same as figure 3.14, but for the Oct.14 control simulation.	25
3.17	Same as figure 3.13, but for the Nov.02 control simulation.	26
3.18	Same as figure 3.14, but for the Nov.02 control simulation.	27
4.1	A budget of cloud water mixing ratio, r_c , for the Nov.11 control simulation. The budget is integrated over a one-hour period from $t = 91$ min to $t = 150$ min. The solid line indicates the overall change in r_c during the observed period. Symbols represent the effect on r_c due to individual model processes. Positive values indicate a source of liquid water, while negative values indicate a sink of liquid water.	33
4.2	Same as figure 4.1, but for the Oct.14 control simulation.	34
4.3	Same as figure 4.1, but for the Nov.02 control simulation.	35
4.4	A budget of snow mixing ratio, r_S , for the Nov.11 control simulation. The budget is integrated over a one-hour period from $t = 91$ min to $t = 150$ min. The solid line indicates the overall change in r_S during the observed period. Symbols represent the effect on r_S due to individual model processes. Positive values indicate a source of snow mixing ratio, while negative values indicate a sink of snow mixing ratio. Processes such as large-scale ascent and radiation do not have a direct effect on snow in our simulations. Therefore, these terms are not included in the snow budget.	36
4.5	Same as figure 4.4, but for the Oct.14 control simulation.	37
4.6	Same as figure 4.4, but for the Nov.02 control simulation.	38
6.1	A scatter plot comparing calculated results from the right-hand side of ((5.20), x-axis) versus the left-hand side obtained directly from the COAMPS-LES sensitivity simulations (y-axis). The solid line indicates equality between the compared values. Points to the left of the line show that our formula underestimates snow precipitation flux, while points to the right of the line show our formula overestimates snow precipitation flux. Symbols denote the cloud case being observed and which sensitivity parameter is being varied.	49
6.2	Same as figure (6.1), but comparing calculated snow precipitation flux from (5.23, x-axis) versus simulated snow precipitation flux (y-axis).	50

LIST OF TABLES

5.1	A list of symbols used to derive diagnostic equations (5.20) and (5.23). Units and values correspond to those used in our control simulations. . . .	45
6.1	Imposed sensitivity values of large-scale vertical velocity (V_{ls}) for each cloud case. Positive values indicate ascent. In each sensitivity study, a single value of ascent or descent is selected. All other parameters are set to their control values. An asterisk denotes the control setting for each cloud case.	48
6.2	Imposed sensitivity values of a'' and N_{0S} . Only one variable is modified for each of these sensitivity cases, while the other variable is set to the control value. An asterisk denotes the control setting for each cloud case. .	48

ACKNOWLEDGEMENTS

First, I would like to thank Dr. Vincent E. Larson for advising me on this project. Over the past four years, Dr. Larson has always treated me with professionalism and endless patience. I do not believe this project would have succeeded without his guidance and support. I would also like to thank the other professors in the UW-Milwaukee Atmospheric Science group. Each professor has taught me so many useful lessons, both inside and outside the classroom. The knowledge that I have gained will stay with me for many years to come.

Many thanks go to my fellow researchers at UW-Milwaukee, especially Michael Falk, Brian Griffin, Dave Schanen, Brandon Nielsen, and Joshua Fasching. They have all worked with me on resolving various research issues, and that help is greatly appreciated. Also, thanks to my fellow graduate and undergraduate students, who have helped provide many laughs and useful discussions during the tough times.

I also need to thank those who have provided me with critical information during this study, including Dr. Larry Carey (ESSC / University of Alabama Huntsville) and Dr. Jianguo Niu (Texas A&M University) for providing aircraft observations, and Dr. J. Adam Kankiewicz for providing LBF rawinsonde data. Dr. Jean-Christophe Golaz (NOAA / GFDL) has been invaluable in providing developmental assistance with the COAMPS-LES model. A special thank you also goes out to Dr. Thomas Vonder Haar at CIRA / Colorado State University for funding this research study, and also for allowing me to directly observe aircraft observations during the CLEX-10 field experiment in Ottawa, Ontario, Canada. These experiences have helped me further understand many of the aspects of cloud studies and meteorology as a whole.

Finally, I would like to thank my parents for constantly supporting my dreams,

no matter what they might be. Most of all, I would like to thank my fiancé, Apryle. She has unselfishly supported me at every turn. I would not have been able to complete this project without her.

COPYRIGHT NOTICE: COAMPS® is a registered trademark of the Naval Research Laboratory.

Chapter 1

Introduction

Midlevel “alto” clouds, such as altostratus or altostratocumulus (Larson et al., 2006), are thin clouds, typically less than 1000m thick. The clouds are generally overcast, meaning that they have cloud fractions of nearly one. In addition, alto clouds may contain both liquid and ice particles, meaning they could be “mixed-phase”. They can occur in any climate region (Sassen and Khvorostyanov, 2007), and they cover up to 22% of the planet’s surface at any given time (Warren et al., 1988a,b).

Because of their prevalence, the clouds can have a significant effect on the surface radiation budget in both climate models and general circulation models (GCMs). A major problem in these models is the prediction of cloud phase, or whether a cloud consists of supercooled liquid, ice particles, or both. Prediction of cloud phase can lead to significant differences in model results. For example, Fowler et al. (1996) note that in GCMs, the liquid and ice phases have different optical properties, and they also undergo significantly different microphysical and thermodynamical processes. Also, Ackerman and Co-Authors (2004) states that cloud feedbacks in climate models can be improved by improving the prediction of phase at temperatures between 0°C and -40°C. Therefore, by producing accurate representations of liquid and ice in mixed-phase clouds, models can then produce better calculations of radiation, cloud behavior and precipitation. In turn, forecasters would then see significant improvements in model predictions.

Mixed-phase clouds can also have a significant effect on small aircraft, such as unmanned aerial vehicles (UAVs). During Operation ENDURING FREEDOM between October 2001 and February 2002, three or more Predator aircraft crashed

in Afghanistan due to icing and bad weather conditions (Haulman, 2003). Predators and other UAVs typically operate in the altitudes where alto clouds exist. In addition, Cober and Isaac (2002) found that during several field projects involving aircraft measurement of icing environments, 48% of the environments in the temperature range from 0°C to -30°C were mixed-phase. Therefore, it is important to understand the phase conditions within mid-level clouds, in the hopes of reducing risk to aviation and military operations.

Despite the importance of understanding mid-level mixed-phase clouds, they are often described as “forgotten clouds” (Vonder Haar and Co-Authors, 1997), because they are studied far less than boundary layer clouds or cirrus clouds. Larson et al. (2006) note that fewer than 100 abstracts or titles on the Science Citation Index (<http://portal.isiknowledge.com/>) contain the words “altocumulus” or “altostratus”. A similar search for the terms “stratocumulus” or “cirrus” resulted in over 1000 results for each keyword. Also, Zhang and Co-Authors (2005) find that general circulation models (GCMs) greatly underpredict thin alto clouds, while overpredicting thicker clouds like nimbostratus. Therefore, additional studies are necessary to accurately predict alto clouds and their phase in numerical models.

To understand microphysical properties within mixed-phase alto cloud layers, this study examines three alto clouds that were sampled by aircraft. In doing so, we specifically ask, “Can we determine cloud phase properties in a simple, yet informative way?” We simulate each cloud using a three-dimensional model and the Large-Eddy Simulation (LES) method. This method allows us to produce high-resolution results with limited parameterization. We also include a full microphysics scheme to simulate both liquid and frozen phases. Using the simulation data, we generate budgets to analyze the evolution of snow and liquid water mixing ratio. These budgets provide details on which microphysical processes are dominant in producing frozen or liquid phase within a cloud. We also wish to determine whether it is possible to

predict the amount of snow formation occurring within a cloud. Using information from our budgets, we produce a new set of equations that attempt to predict snow mixing ratio and snow precipitation flux at the base of a cloud. These formulas are compared with the results of a sensitivity study in order to verify their accuracy.

Chapter 2

Model description

For this study, we use the Coupled Ocean/Atmosphere Mesoscale Prediction System (COAMPS®) Large-Eddy Simulation (COAMPS-LES) model (Golaz et al., 2005). This model has been previously used for high-resolution, three-dimensional LES studies of observed midlevel altostratocumulus cases (Larson et al., 2006; Falk and Larson, 2007). A detailed description of the model is available in Hodur (1997), and optional settings used in this study are detailed in Larson et al. (2006).

All of our simulations use a horizontal grid spacing of 75 m x 75 m, and a vertical grid spacing of 25 m. The horizontal domain size is 4125 m x 4125 m. Because we are simulating multiple cloud cases, the vertical domain size ranges from 3000 to 4500 m, with each of our three simulations using a different vertical extent. For specific vertical domain sizes, see the individual case descriptions below. Because the cloud systems are all isolated from the boundary layer, surface and momentum fluxes at the lower model boundary are set to zero. Time step is 1 s, with a total simulated time of 4 h for all cases.

The net vertical longwave radiative flux is calculated following Stevens and Co-Authors (2005). To calculate shortwave radiation, we use the two-stream, single-band model of Shettle and Weinman (1970) and Duynkerke and Co-Authors (2004). A description of these formulas and the corresponding radiative constants are described in Larson et al. (2007). We also apply large-scale ascent or descent to individual simulations by selecting a constant vertical velocity and using it to advect water vapor, potential temperature and horizontal winds in the vertical. The values of ascent or descent are provided in the individual cloud case descriptions.

2.1 A single-moment microphysical scheme

COAMPS-LES uses a single-moment bulk microphysical scheme based on Rutledge and Hobbs (1983). Detailed information on the microphysical equations can be found in Long (2003). The scheme predicts the mixing ratio of five hydrometeor species: cloud water (r_c), rain (r_r), snow (r_s), cloud ice (r_i), and graupel (r_g). Microphysical effects on potential temperature (θ) are also calculated. In all of our cloud cases, aircraft observations show no evidence of graupel, rain, or drizzle, so we deactivate these related processes in our model.

Explicit equations are provided for the microphysical processes, which include homogeneous freezing of liquid and vapor, ice nucleation, depositional growth, and collection. The scheme does not include a calculation for aggregation. We find that in the aircraft observations, aggregates did appear, but our simulations reproduce accurate cloud conditions without including this process. After all microphysical calculations are completed, the adjustments are applied to the mixing ratio of each hydrometeor species, and the potential temperature is modified to account for latent heating from phase changes.

In our simulations, we calculate ice particle number concentration using formulas from Fletcher (1962) and Cooper (1986). At each grid point where microphysics is applied, the ice number concentration is calculated from each formula, and the largest diagnosed concentration is used. We have tested alternative ice nucleation formulas, such as Meyers et al. (1992) and the individual Fletcher and Cooper formulas. Our results have revealed that the combined Fletcher/Cooper method generates the most accurate snow conditions for our study (not shown).

It must be noted that the Fletcher and Cooper formulas calculate ice number concentration as a diagnostic function of temperature. The formulas do not determine whether a grid point is saturated or subsaturated with respect to ice. Therefore, our method does not include any sinks of ice nuclei, leading to a potentially limitless

source of these particles. However, in natural conditions, ice number concentration in a region may actually decrease due to precipitation, phase changes, or other processes. We find that in our models, the calculation of number concentration does not produce a significant source of error (see below).

Furthermore, single-moment schemes may produce less accurate simulations than double-moment bulk microphysics methods (e.g., Ferrier, 1994; Morrison et al., 2005) or bin microphysical methods (e.g., Reisin et al., 1996; Lynn et al., 2005). These schemes allow for detailed prediction of snow particle size, shape and fall speed. However, the goal in this study is to produce a method that provides a simple analysis of mixed-phase cloud behavior. We find that the single moment scheme allows us to obtain an analytic formula that satisfies our goal, while retaining a reasonable degree of accuracy in our results.

Chapter 3

The Cloud Cases

For this study, we simulate three mixed-phase alto clouds that were observed by aircraft. Each of these clouds was thin, and the liquid of each cloud is less than 1000 m in thickness. All three clouds could be described as “altostratocumulus” (Larson et al., 2006), meaning they were overcast (analogous to “stratocumulus” clouds) and they are also isolated from the boundary layer (thus classifying these systems as “alto” clouds). In all of our studied clouds, peak liquid occurs primarily at cloud top, while maximum ice appears at lower altitudes within the mixed-phase region. This behavior is consistent with observations in Fleishauer et al. (2002) and sources cited therein.

3.1 The Nov.11 cloud

We first simulate a cloud that was sampled by an aircraft over central Montana on 11 November 1999. This cloud was sampled during the fifth of the Complex Layered-Cloud Experiments (CLEX-5). Descriptions of the aircraft, instrumentation and corresponding observations are provided in Fleishauer et al. (2002). The thickness of the liquid cloud was measured to be approximately 500 m. For this cloud, the thickness of the cloud ice and virga layer was not measured by aircraft.

The Nov.11 cloud was the subject of a three-dimensional LES simulation study in Larson et al. (2006). In the previous study, a simplified ice parameterization was used to simulate depositional growth of ice, because the authors of the study only wished to study effects on the liquid portion of the cloud. However, we now wish to focus on snow and the factors that affect its growth. Therefore, it is necessary to

use a full microphysical scheme.

In order to completely simulate the microphysical processes in and near the cloud region, the simulated vertical domain is now increased to 4400 m from the previous study's vertical domain of 2400 m. The model base is now placed at 3000 m above mean sea level. In our simulations, large-scale descent is set to 3 cm s^{-1} (Larson et al., 2006). To calculate shortwave radiation, the solar zenith angle is set to a constant value, since the observation period occurred around midday. Other radiative constants for this simulation are the same as in Larson et al. (2006).

3.2 The Oct.14 cloud

We also simulate a cloud sampled during the ninth of the Complex Layered-Cloud Experiments (CLEX-9). This cloud has been observed to have similar liquid water and ice structure to the Nov.11 cloud.

The cloud was observed on 14 October 2001 near North Platte, NE (Kankiewicz et al., 2006). The cloud formed before sunrise, and the aircraft sampled the cloud region between 1210 and 1600 UTC. The observed cloud top temperature was approximately -22°C . A second sampling period was performed from 1715 to 1900 UTC, indicating the cloud layer persisted for a significant length of time. As with the Nov.11 cloud, peak liquid water occurs at cloud top, with cloud ice and virga extending approximately 2000 m below the liquid layer. The liquid layer in the cloud was approximately 800 m in thickness, with the layer centered at 5000 m above mean sea level.

The Oct.14 cloud was sampled with the University of Wyoming's King Air aircraft. A spiral sounding and two leg soundings were completed during the sampling period. Instruments used during the sampling included 2-DC and 2-DP for measuring the size distribution of ice particles, FSSP, upward- and side-looking Wyoming Cloud Radar, and probes to measure the thermodynamic and aircraft geographic

location (Niu et al., 2006).

In this cloud case, in-situ sampling was limited to the cloud region and regions of corresponding ice virga. Therefore, thermodynamic information above and below cloud was not available. However, in order to simulate cloud-top entrainment and microphysical processes accurately, additional sounding data is necessary. This data was obtained from a special rawinsonde launched during the aircraft flight. The rawinsonde was launched from the National Weather Service's North Platte, NE office, located at the Lee Bird Field (LBF) airport. Because the rawinsonde was launched approximately 45 miles from the aircraft sampling region, the resulting sounding does not sample the region directly observed by aircraft. However, it does provide sufficient temperature, wind and moisture information in order to produce a reasonable simulation.

To simulate the cloud region fully, the simulated vertical domain is 4500 m, with the model base located at 2213 m above mean sea level. Because the Oct. 14 cloud was observed at roughly the same latitude and longitude as the Nov.11 cloud, we use the same longwave radiation constants provided in Larson et al. (2006). However, since the Oct.14 cloud was first observed at sunrise and the plane sampled the cloud during mid-morning, we must apply a widely varying solar zenith angle to account for increasing solar radiative flux as the simulated period progresses. We use the methodology of Liou (2002) to calculate the solar zenith angle needed at each individual time step.

Both the aircraft observations and the supplemental sounding indicate strong vertical wind shear. To duplicate the wind shear in our simulations, we obtain the aircraft-observed wind profile in both horizontal directions, and then subtract the mean wind to produce a wind profile relative to cloud motion. In addition, the persistence of the observed cloud layer indicates the presence of large-scale ascent in the region. Therefore, this ascent must also be applied to the simulation. A value

of 1.4 cm s^{-1} was obtained using data from the National Centers for Environmental Prediction (NCEP) North American Regional Reanalysis (NARR). The times selected for this data were 1200 UTC and 1500 UTC on 11 October 2001. Like the Nov.11 case, this velocity was applied over the model domain in order to vertically advect the prognostic variables and horizontal wind fields.

3.3 The Nov.02 cloud

For a third cloud study, we simulate a mixed-phase cloud observed on 02 November 2001 during the CLEX-9 experiment (Kankiewicz et al., 2006). This cloud was sampled between 1220 UTC and 1620 UTC. After 1600 UTC, the cloud layer was observed to begin breaking up, with complete dissipation by 1730 UTC (not shown). Observations indicate that the Nov.02 cloud top temperature was nearly -13°C , which is 9 degrees warmer than the Oct.14 cloud. Therefore, it appears that the warmer temperatures limited the amount of liquid and ice generated in this case. These conditions likely contributed to the cloud dissipation after the aircraft sampling period was completed.

Like the Nov.11 and Oct.14 clouds, the Nov.02 cloud contains peak liquid at the top of the layer, with ice predominant at lower altitudes. The liquid cloud has a 400m vertical extent centered at approximately 4100 m, while ice extends approximately 1500 m below the liquid layer. Because the Nov.02 cloud was observed as part of the CLEX-9 experiment, the aircraft instruments and sampling methods are the same for the Nov.02 and Oct.14 cases. Since the in-situ observations are available only within cloud, we must again use a supplemental sounding launched from LBF during the observation period. Like the Oct.14 case, the Nov.02 case was sampled approximately 45 miles from the LBF site, but the supplemental sounding provides reasonable information on the atmospheric conditions above and below cloud. Vertical wind profiles obtained from aircraft and supplemental soundings

indicate that this case had strong vertical wind shear, so we apply a relative wind profile similar to the one used in the Oct.14 case.

For this case, the simulated vertical domain was 3000 m, with model base located at 3097 m above mean sea level. The Nov.02 cloud was sampled in nearly the same geographic location as the Oct.14 case, so the same radiation constants were selected for consistency. Also, the Nov.02 cloud initially developed around sunrise and persisted through the morning. Therefore, a varying solar zenith angle is used in our simulation. Finally, to obtain an accurate value of large-scale ascent, we again use the NCEP North American Regional Reanalysis. A velocity of 0.7 cm s^{-1} was obtained using data obtained from 1200 UTC and 1500 UTC on 02 November 2001.

3.4 Comparisons of the simulated profiles versus aircraft data

To verify our initial profiles match the observed profiles, we now present vertical profiles of moisture and temperature for each cloud case. In order to match observations, we set the initial vertical profiles of liquid and temperature, then run the model. The first hour of simulation acts as a spinup period to generate turbulence and radiative effects. Once this period is completed, we examine the simulated profiles at $t = 61 \text{ min}$, in order to verify that the simulated conditions match observations.

In the study, all simulated vertical profiles are horizontally averaged for simplicity. In the aircraft soundings, the mixing ratio profiles are jagged, indicating variability in either the horizontal or vertical. The three-dimensional model does account for horizontal variability, but in order to obtain a single vertical profile, horizontal averaging must be applied. We find that the resulting averaged profiles still produce accurate in-cloud conditions, and are reasonable for comparison with

aircraft data.

For each cloud case, we now present profiles of liquid water mixing ratio (r_c , figures 3.1-3.3), water vapor mixing ratio (r_v , figures 3.4-3.6), and potential temperature (θ , figures 3.7-3.9). The solid line represents the Lagrangian spiral sounding observed at the beginning of the sampling period. The dotted lines represent the simulated profiles taken immediately after the model spinup is completed. In the comparisons of potential temperature, the additional dashed line (figures 3.8-3.9) denotes the supplemental rawinsonde soundings, which are used to extend our simulated sounding in the absence of aircraft measurements in the Oct.14 and Nov.02 cases. We do not plot the rawinsonde data in comparisons of mixing ratio, because the corresponding soundings do not include the measurements of cloud water or water vapor that would be required.

As the comparison figures show, each simulation is specifically set up so our simulated profiles match the aircraft observations as closely as possible. We do find that the simulated r_v is smaller than the aircraft-measured r_v for both the Oct.14 and Nov.02 cases (figures 3.5 and 3.6). To explain why, we also plot the simulated saturation mixing ratio with respect to liquid at $t = 61$ min (stars). This profile indicates that our cloud region becomes saturated at a lower mixing ratio than the aircraft sounding indicates. If we added more vapor to match the aircraft data, the excess vapor would immediately be converted to cloud water. Therefore, because we still closely match the cloud water profiles in our simulations to the observed results, our water vapor profiles are acceptable for this study.

During model setup, we do not manually set the initial snow mixing ratio. Instead, we allow the microphysics scheme to calculate the snow fields. Therefore, we must verify that our microphysics scheme is accurately simulating snow conditions. Comparisons of simulated snow mixing ratio (r_s) versus actual conditions are shown in figures 3.10-3.12. The solid line represents the simulated snow profile, while the

symbols represent snow mixing ratios obtained from the aircraft soundings. Because snow conditions vary greatly in the observations, we display the results from all available soundings for each case. The Nov.11 case had one sounding with a vertical profile of snow mixing ratio, while the Oct.14 and Nov.02 cases had three soundings each.

It must be noted that during the first 20 minutes after microphysics is activated, a large burst of snow is generated in our simulations. During this period, the microphysics scheme generates the frozen precipitation, then the corresponding fields are allowed to come to equilibrium. To account for this extra spinup, we obtain our simulated snow profiles at $t = 90$ min. We find that after this simulation time, snow evolves in a realistic manner for all of our cloud cases.

The accuracy of the microphysics scheme varies with each simulation. For example, figure 3.11 shows that the thickness of the Oct.14 simulated snow layer is well represented, and the simulation produces a snow profile within the spread of all sounding results. Meanwhile, figure 3.10 and figure 3.12 both show that the microphysics overestimates the thickness of the snow layer. However, all simulated profiles produce a reasonable amount of snow mixing ratio, especially within cloud.

The difference between the simulation profile and observations in figures 3.10 and 3.12 can be explained in two ways. First, the aircraft observations indicate a strong horizontal variability in the snow mixing ratio, due to the wide range of mixing ratios over a limited vertical extent. Due to the horizontal averaging in our profiles, this variability is removed from our results, leading to a mean profile does not exactly match observations. In addition, while the Nov.11 and Nov.02 cases produce snow below the observed region, the aircraft only sampled regions very close to the cloud boundary. Because the aircraft did not sample the below-cloud precipitation, it is possible that the precipitation was present during the sampling period. Therefore, we accept the simulated snow profiles for this study.

3.5 Time evolution of liquid and snow

The final way to examine the cloud results is to observe their evolution over an extended period of time. To understand the phase of these clouds, we need to examine how the liquid and snow evolve. In this way, we can then begin to devise methods to study this evolution.

We now examine the evolution of liquid water and snow for each simulation. The Nov.11 cloud is shown in figures 3.13-3.14, the Oct.14 case is shown in figures 3.15-3.16, and the Nov.02 case is shown in figures 3.17-3.18.

One interesting finding from these figures is that in our model, falling snow appears as low as 3000 m below the liquid cloud region. This indicates the presence of a large below-cloud region of supersaturation with respect to ice. The depth of the snow virga in our simulations appears to be related to when our vapor profile becomes subsaturated with respect to ice. However, the depth of the ice virga layer does not appear to influence the evolution of the cloud or its phase.

The figures also alleviate a potential concern with our microphysics scheme. As mentioned earlier, our calculation of ice particle number concentration is dependent only on temperature. Therefore, the simulations could potentially generate an infinite source of ice nuclei that would allow excessive amounts of snow to form. In our simulations, however, we do not see a dramatic increase in the snow mixing ratio over time. This indicates that although infinite sources of ice nuclei may be present, the model still generates snow in a manner consistent with natural conditions.

While the time evolution provides an interesting look at how the clouds evolve, the figures do not provide insight into what processes are generating liquid or snow. Therefore, other methods must be devised to provide additional information for our study.

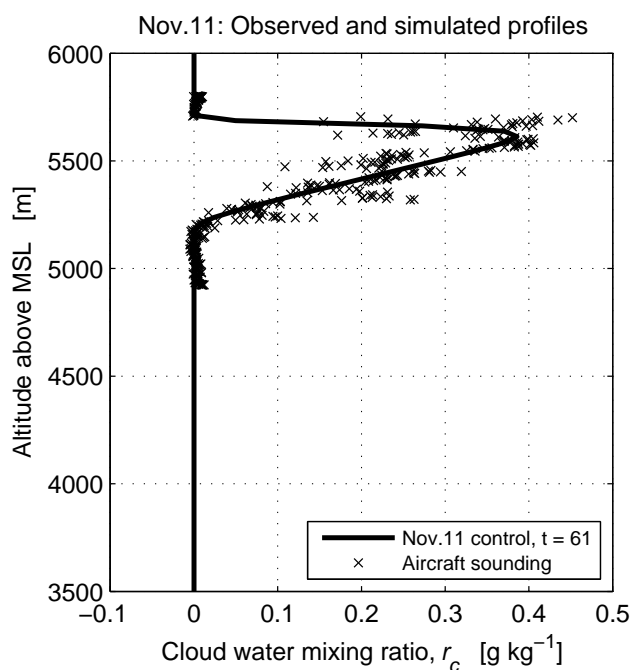


Figure 3.1: A comparison of simulated liquid water mixing ratio (r_c) in the Nov.11 control simulation versus the available aircraft sounding. A solid line denotes the simulated profile, while symbols represent the observed aircraft conditions. The simulated profile is obtained at $t = 61$ min, immediately after the model spinup period is completed.

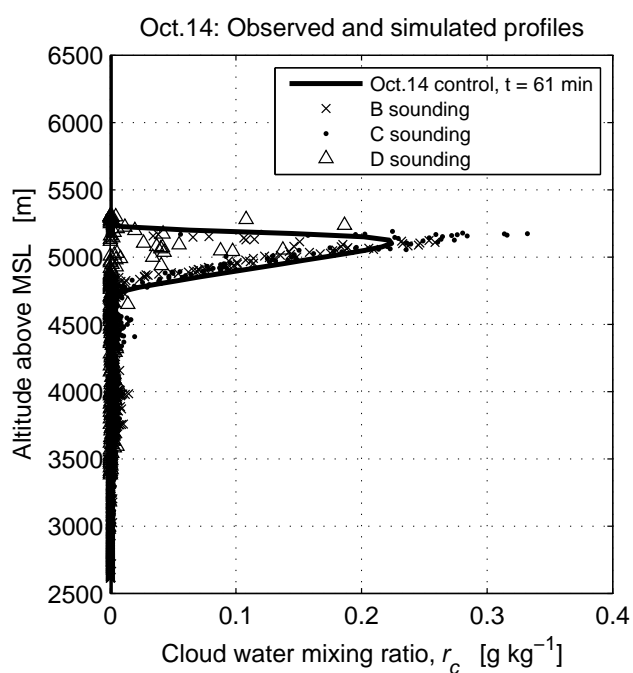


Figure 3.2: Same as figure 3.1, except for the Oct.14 control simulation. Here, three different symbols are used to denote data from all three available aircraft soundings.

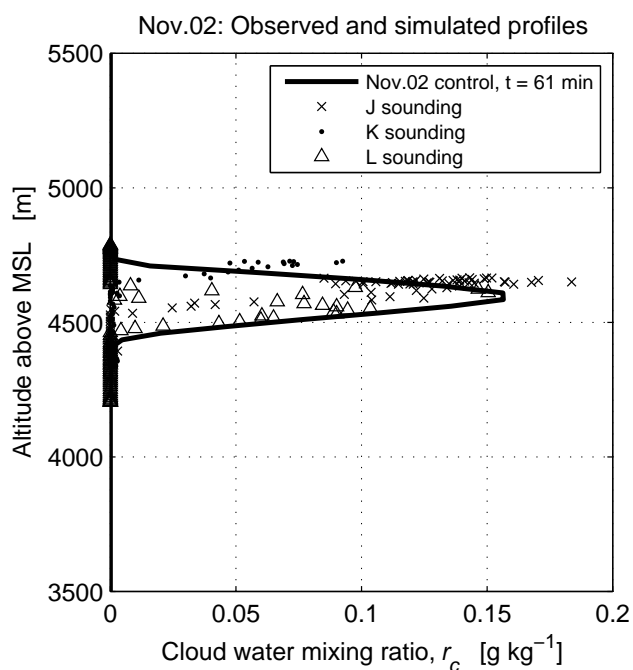


Figure 3.3: Same as figure 3.2, except for the Nov.02 control simulation.

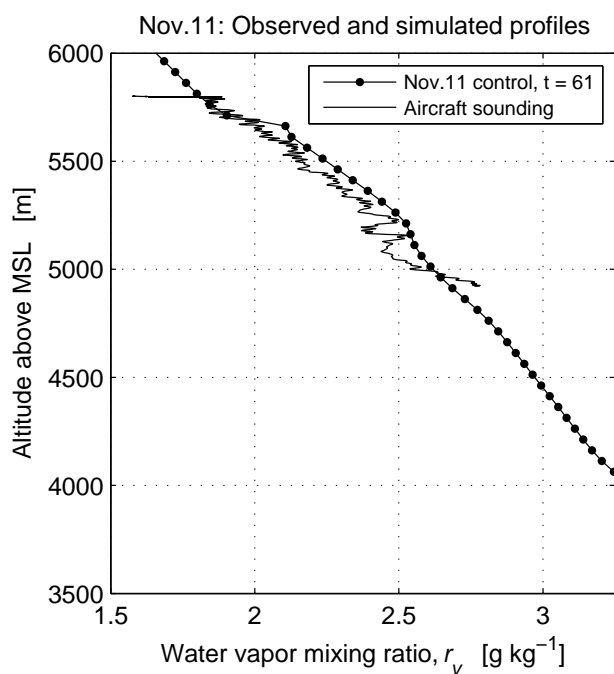


Figure 3.4: A comparison of simulated water vapor mixing ratio (r_v) in the Nov.11 control simulation versus the available aircraft sounding. Dots represent the simulated profile, while a thin line indicates the observed aircraft profile. The simulated profile is obtained at $t = 61$ min, immediately after the model spinup period is completed.

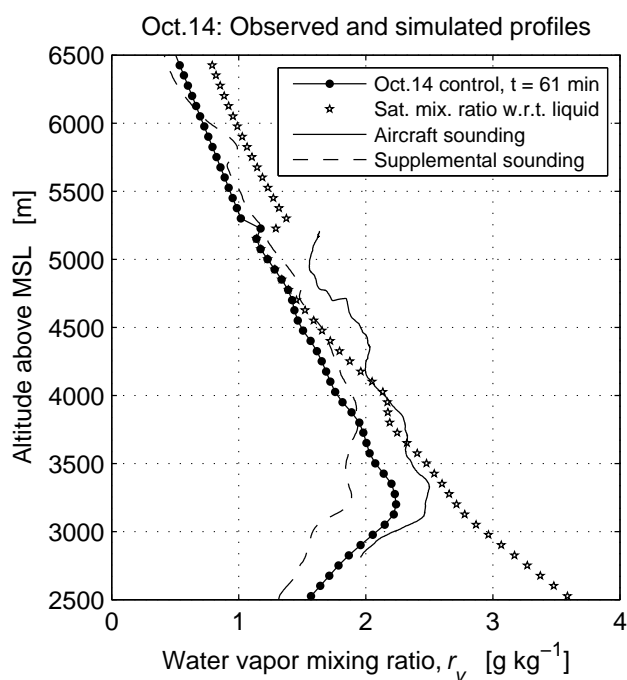


Figure 3.5: Same as figure 3.4, except for the Oct.14 control simulation. A supplemental rawinsonde sounding (dashed line) is included to verify that the simulated above- and below-cloud profile matches environmental conditions where the aircraft sampling did not occur. The simulated saturation mixing ratio at $t = 61$ min is also provided (stars), to demonstrate the saturation conditions within our simulation.

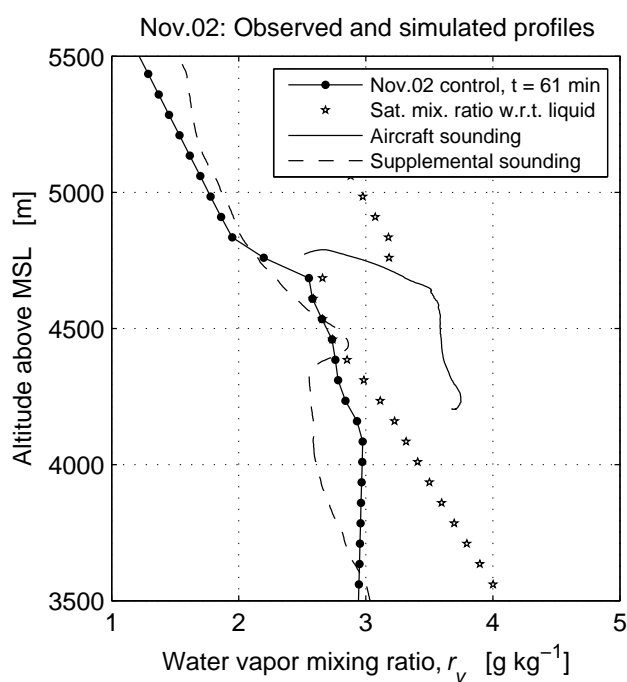


Figure 3.6: Same as figure 3.5, except for the Nov.02 control simulation.

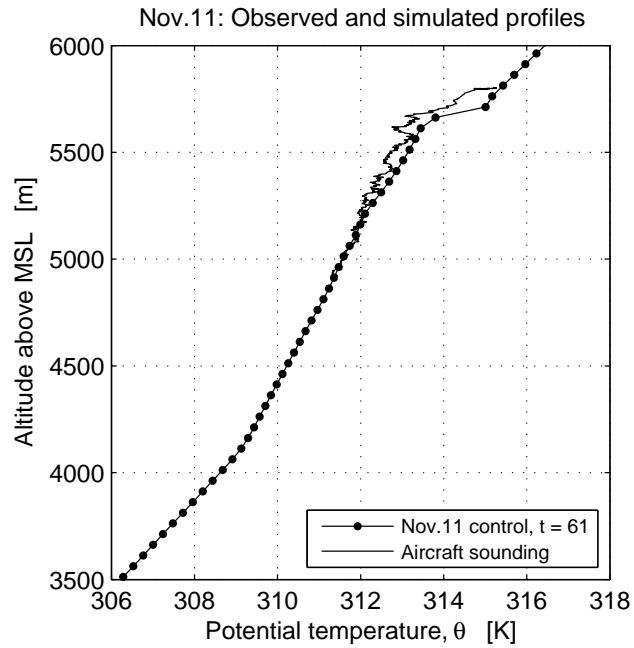


Figure 3.7: A comparison of simulated potential temperature (θ) in the Nov.11 control simulation versus the available aircraft sounding. Dots represent the simulated profile, while a thin line indicates the observed aircraft profile. The simulated profile is obtained at $t = 61$ min, immediately after the model spinup period is completed.

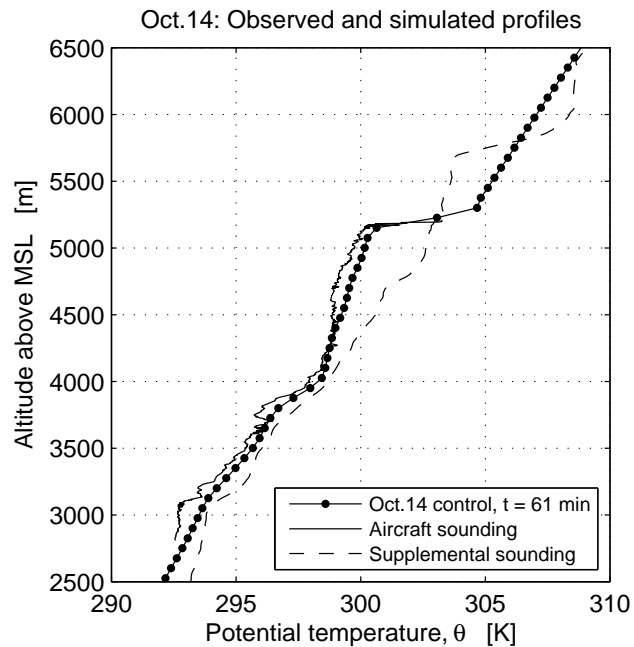


Figure 3.8: Same as figure 3.7, except for the Oct.14 control simulation. A supplemental rawinsonde sounding (dashed line) is included to verify that the simulated above- and below-cloud profile matches environmental conditions where the aircraft sampling did not occur.

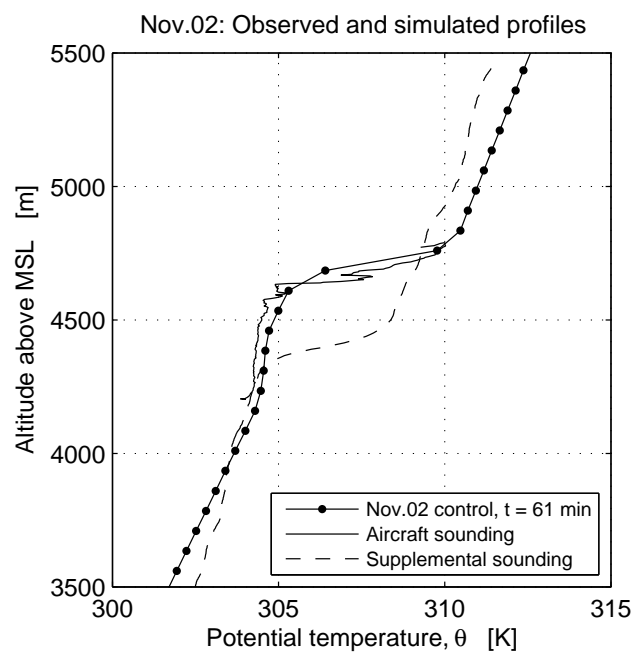


Figure 3.9: Same as figure 3.7, except for the Nov.02 control simulation.

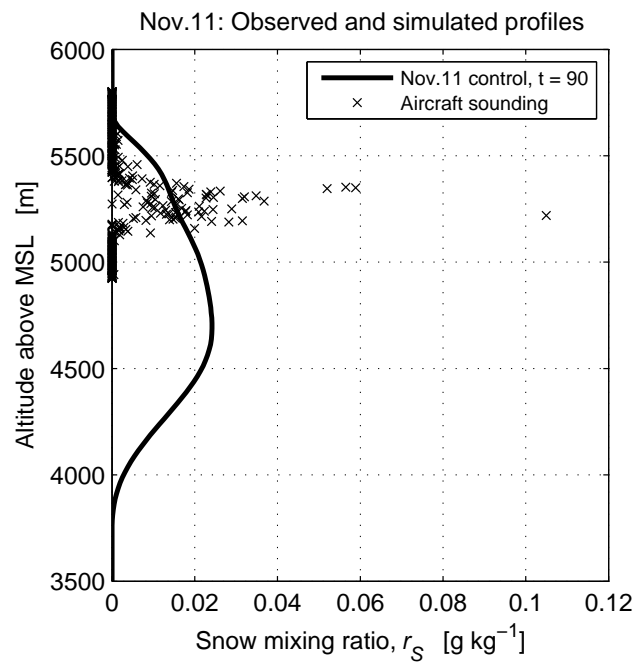


Figure 3.10: A comparison of simulated snow mixing ratio (r_s) in the Nov.11 control simulation versus the available aircraft sounding. A solid line denotes the simulated profile, while symbols represent the observed aircraft conditions. The simulated profile is obtained at $t = 90$ min, to account for a spinup period for the microphysics scheme.

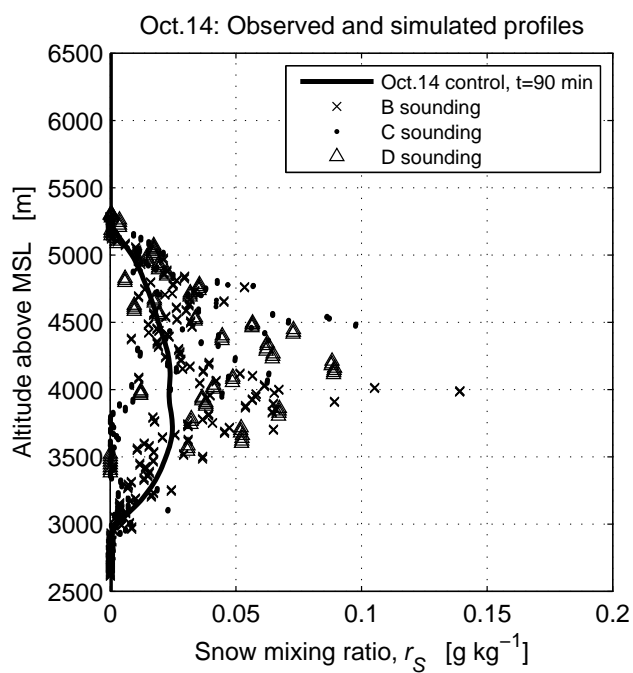


Figure 3.11: Same as figure 3.10, except for the Oct.14 control simulation. Here, three different symbols are used to denote data from all three available aircraft soundings.

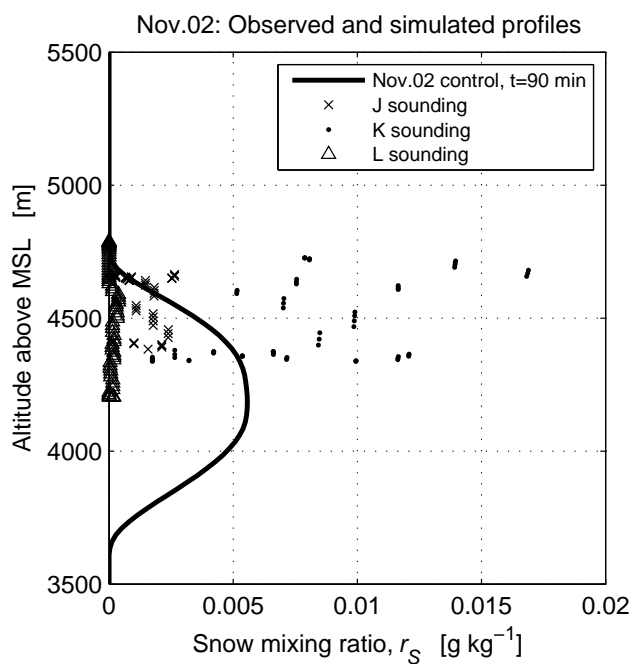


Figure 3.12: Same as figure 3.11, except for the Nov.02 control simulation.

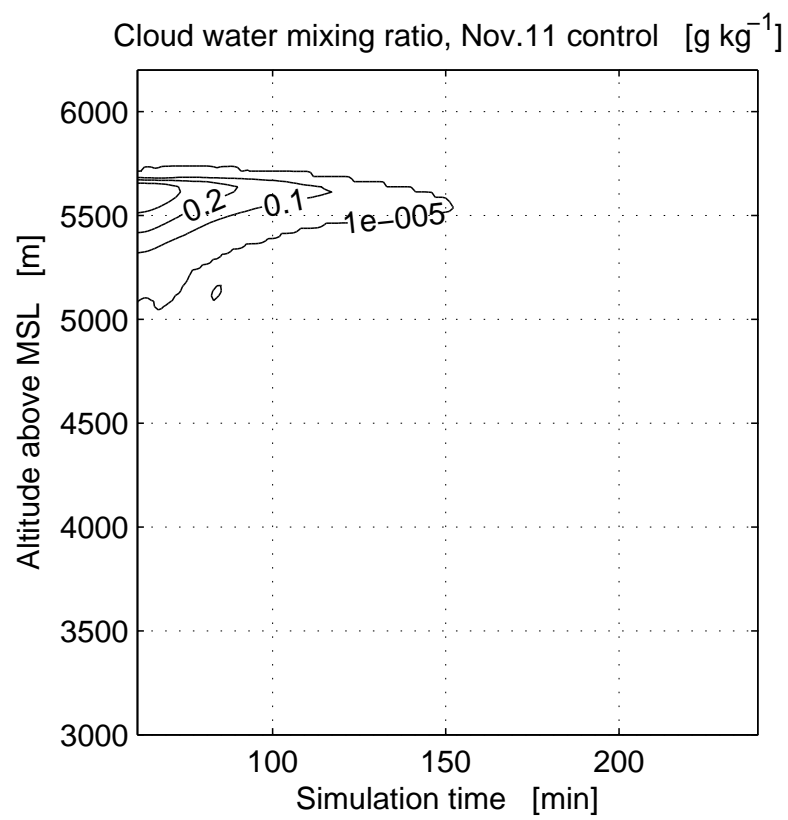


Figure 3.13: A contour plot showing the evolution of liquid water mixing ratio, r_c , for the Nov.11 control simulation.

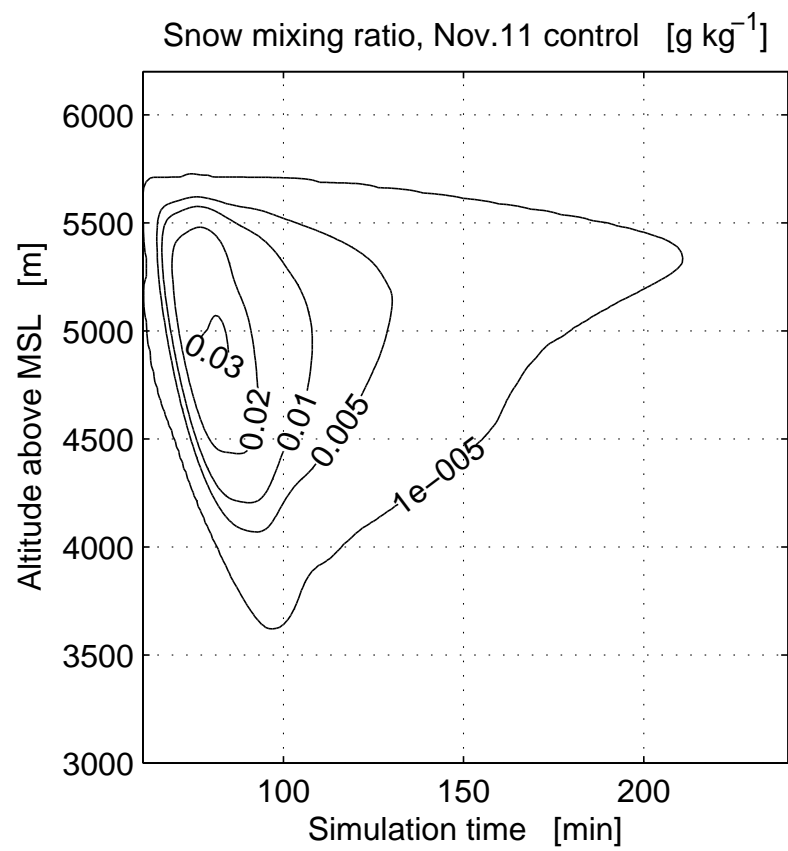


Figure 3.14: A contour plot showing the evolution of snow mixing ratio, r_S , for the Nov.11 control simulation.

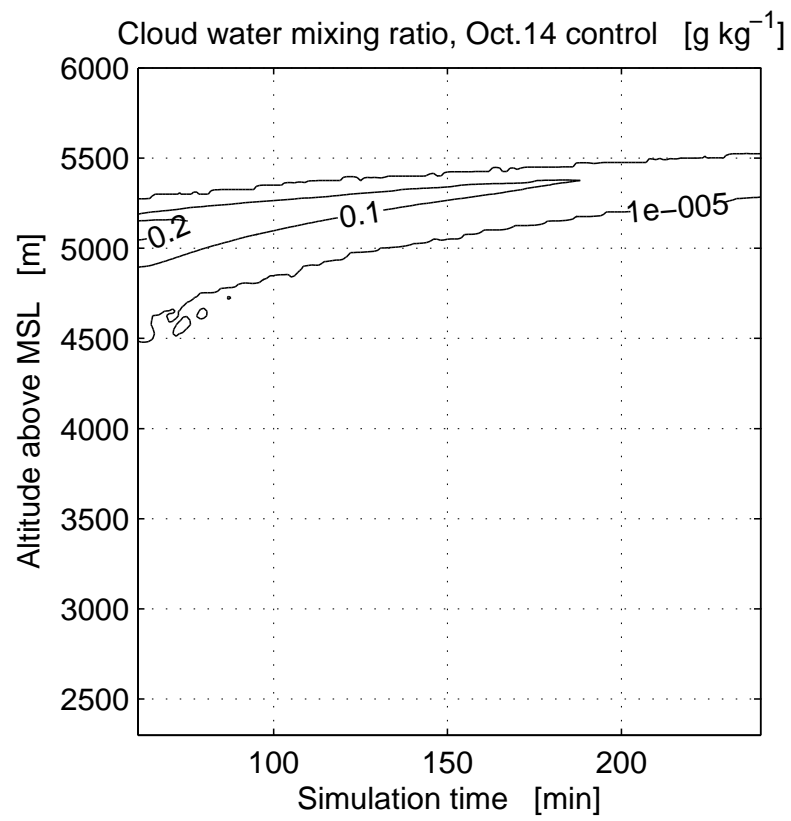


Figure 3.15: Same as figure 3.13, but for the Oct.14 control simulation.

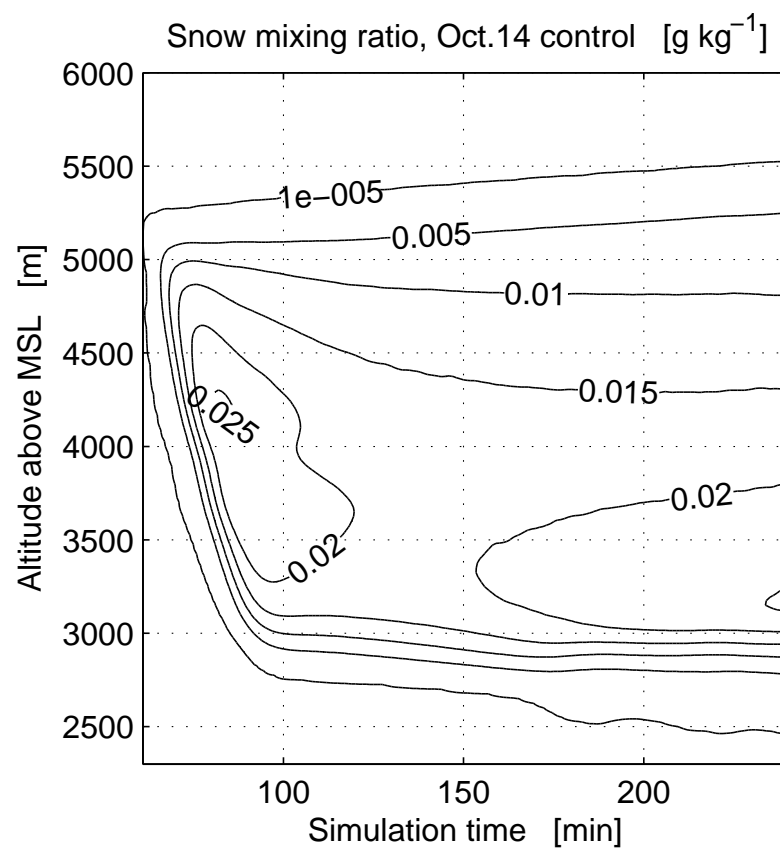


Figure 3.16: Same as figure 3.14, but for the Oct.14 control simulation.

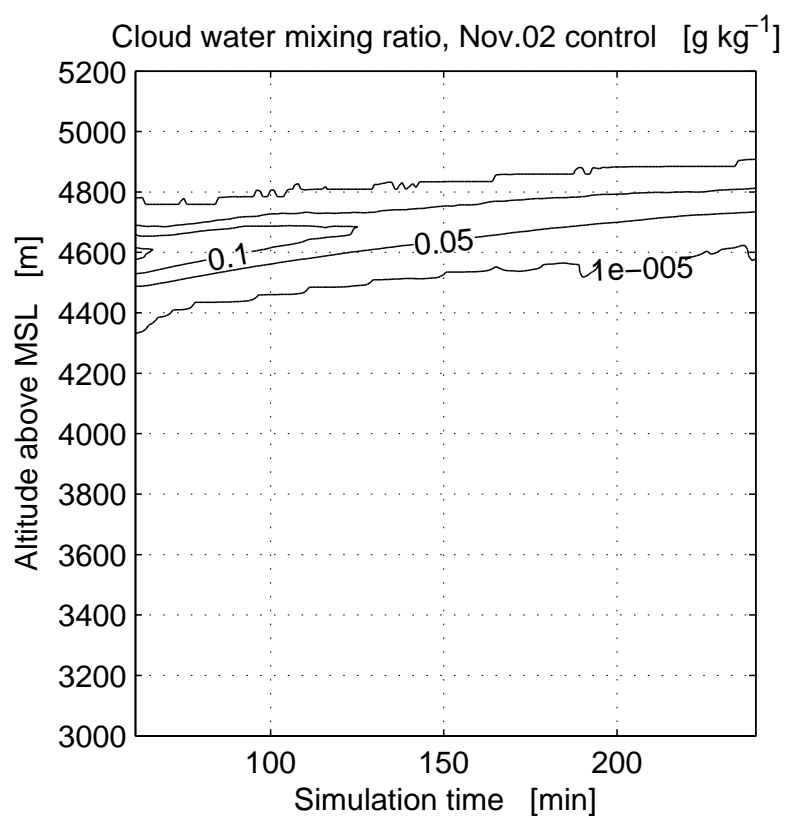


Figure 3.17: Same as figure 3.13, but for the Nov.02 control simulation.

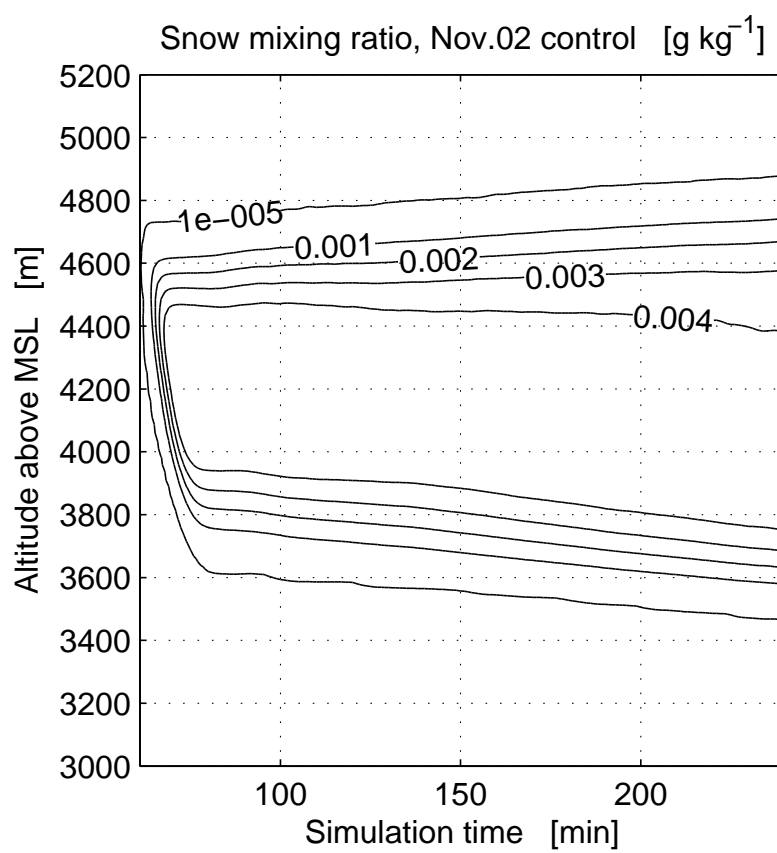


Figure 3.18: Same as figure 3.14, but for the Nov.02 control simulation.

Chapter 4

Budgets showing primary effects on cloud water and snow mixing ratio

We now wish to determine which processes have the greatest effect on the mixing ratios of cloud water (r_c) and snow (r_s) occurring within and below cloud. A large number of thermodynamic and microphysical processes affect the evolution of each species, so it is ideal to calculate an equation that factors in as many processes as possible. To do so, we evaluate budget equations (Stull, 1988; Larson et al., 2006). These budgets allow us to determine the magnitude of each individual process, and determine which processes are most important inside and outside of our cloud regions.

All of our budgets balance completely within roundoff error, so all individual terms sum up to equal the overall change in mixing ratio. In some cases, other terms appear in the budget equation, but are negligible. Our budgets are calculated for each model altitude, and horizontally averaged to produce a single vertical profile. They are also integrated over a period of time, in order to determine the time rate of change in mixing ratio due to each model process.

4.1 A budget for the time evolution of cloud water mixing ratio

A derivation for an example budget equation affecting cloud water mixing ratio is provided in Larson et al. (2006). This budget uses the conserved variables r_t (total

water mixing ratio = liquid + vapor) and θ_l (liquid water potential temperature). We calculate individual budget terms for each conserved variable, and combine the results to form the liquid water (r_c) budget. This method allows us to take general terms, such as condensation and evaporation, and partition them into other thermodynamic effects. By partitioning the processes, we can then view the indirect effects of radiation on liquid. Our conserved budget also allows for the inclusion of microphysical processes. The weakness of the conserved budget method is that in order to use the conserved variables, we must presume that there is no supersaturation or subsaturation in the presence of liquid (see Larson et al., 2006, equation (A4)). Therefore, our budget method requires cloud fraction to be either 0 or 1. However, each of our cloud cases is overcast, and the cloud boundaries were observed to be uniform. Therefore, the conserved budget method is acceptable for this study.

We now present the conserved budget equation for liquid water, with microphysics included:

$$\begin{aligned} \left\langle \frac{\partial r_c}{\partial t} \right\rangle &= \text{Mix}_{r_c} + \text{Ascent}_{r_c} + \text{Rad}_{r_c} \\ &+ \text{PSACW}_{r_c} + \text{PSDEP}_{r_c} + \text{PDEPI}_{r_c}, \end{aligned} \quad (4.1)$$

where Mix_{r_c} is the change in cloud water due to turbulent mixing, Ascent_{r_c} is the change in cloud water due to large scale ascent (or descent), Rad_{r_c} is the change in cloud water due to radiation, PSACW_{r_c} is the amount of cloud water collected by falling snow, PSDEP_{r_c} is the change in cloud water due to depositional growth of snow, and PDEPI_{r_c} is the change in cloud water due to depositional growth of cloud ice.

Results from the conserved cloud water budget are presented for each of the cloud cases in figures 4.1-4.3. Each budget is integrated over the simulated period from $t = 91$ min to $t = 151$ min. Each symbol represents a single model process,

while the solid line indicates the total tendency of cloud water, or the sum of the tendency generated by all individual model processes. For reference, a dashed line indicates the profile of liquid at $t = 91$ min. For each individual budget profile, a positive point indicates the process is generating liquid at that altitude, while a negative point indicates the process is depleting liquid at that altitude.

The total tendency of each cloud varies, depending on conditions. For example, the Nov.11 cloud (figure 4.1) shows liquid is being depleted at all altitudes. The primary contributor to depletion appears to be large-scale descent (diamonds), which is consistent with the observations of Larson et al. (2006). Microphysical effects also provide a significant means of depletion, also consistent with the previous study. The strongest microphysical process is depositional growth of snow (xs), which have a far greater contribution than the other microphysical processes.

The other two cloud cases show a somewhat different trend. Both the Oct.14 and Nov.02 budgets shows a strong depletion of liquid from the cloud base through most of the liquid region, but some liquid is also generated at cloud top. This tendency occurs due to the large-scale ascent that is implemented in these two cases. Here, we again see that depositional growth of snow is a primary means of liquid depletion, with some additional contribution from snow collecting cloud water (squares).

We must explain the mechanism of how depositional growth of snow depletes liquid. The process of depositional growth occurs in an environment supersaturated with respect to ice. Here, water vapor is deposited onto an ice particle. The decrease in water vapor leads to a subsaturated environment with respect to liquid, allowing liquid water to evaporate. Thus, depositional growth of snow can indirectly lead to a decrease in liquid water.

The liquid water budget figures provide an insight into how liquid evolves in out cloud cases. However, they do not describe how snow evolves over time. Therefore, an additional budget must be provided to examine snow.

4.2 A budget for the time evolution of snow mixing ratio

To observe the tendency of snow, we must now produce a new budget equation for the change in snow mixing ratio (r_S). Like the liquid budget, the snow budget includes both microphysical processes and thermodynamic processes. However, snow is not a conserved variable. Therefore, the terms in this budget are obtained directly from the COAMPS-LES model. Therefore, our snow budget is analogous to the “raw” liquid budget presented in Larson et al. (2006).

The budget for the evolution of snow mixing ratio is as follows:

$$\begin{aligned} \left\langle \frac{\partial r_S}{\partial t} \right\rangle &= \text{Mix}_{r_S} + \text{Sediment}_{r_S} \\ &+ \text{PSACW}_{r_S} + \text{PSDEP}_{r_S} + \text{PCONV}_{r_S}, \end{aligned} \quad (4.2)$$

where Mix_{r_S} is turbulent mixing, Sediment_{r_S} is the motion of falling snow, PSACW_{r_S} is the microphysical process of snow collecting cloud water, PSDEP_{r_S} is the microphysical process of depositional growth of snow, and PCONV_{r_S} is the conversion of cloud ice to snow. Here, the term PCONV_{r_S} acts as a source of snow due to the way frozen hydrometeors are classified in our model. In our microphysics scheme, cloud ice and snow are differentiated by particle mass. When a cloud ice particle reaches a specifically large mass, it is converted into snow. Therefore, because snow is generated through this “process”, we must include a corresponding term in the budget. Also, depositional growth is negative below cloud, indicating that snow is sublimating in conditions that are subsaturated with respect to ice. Finally, in our model, large-scale ascent does not have an effect on snow evolution. Therefore, the term is not included in our snow budget.

Results from (4.2) are shown in figures 4.4-4.6. Like the liquid budgets, each snow budget is integrated over the simulated time interval from $t = 91$ min to t

= 150 min. Again, a solid black line shows the total tendency of the snow mixing ratio, while the symbols indicate the contributions made by individual processes.

It can be shown that in all three cloud cases, the evolution of snow mixing ratio is dominated by sedimentation and depositional growth throughout our model domain. Contributions do appear from collection and conversion from cloud ice to snow, but they are negligible when compared to the larger terms. The total r_S tendency is relatively small in the Oct.14 and Nov.02 cases, while the Nov.11 has the largest negative tendency. Overall, the total tendency is relatively small but not insignificant.

Another interesting observation is that in the Oct.14 and Nov.02 cases, sedimentation and depositional growth appear to nearly balance each other out. It is not unreasonable to say that falling snow and depositional growth (or sublimational loss) have a net effect on snow mixing ratio of nearly zero. This property provides a useful insight that we use in chapter 5.

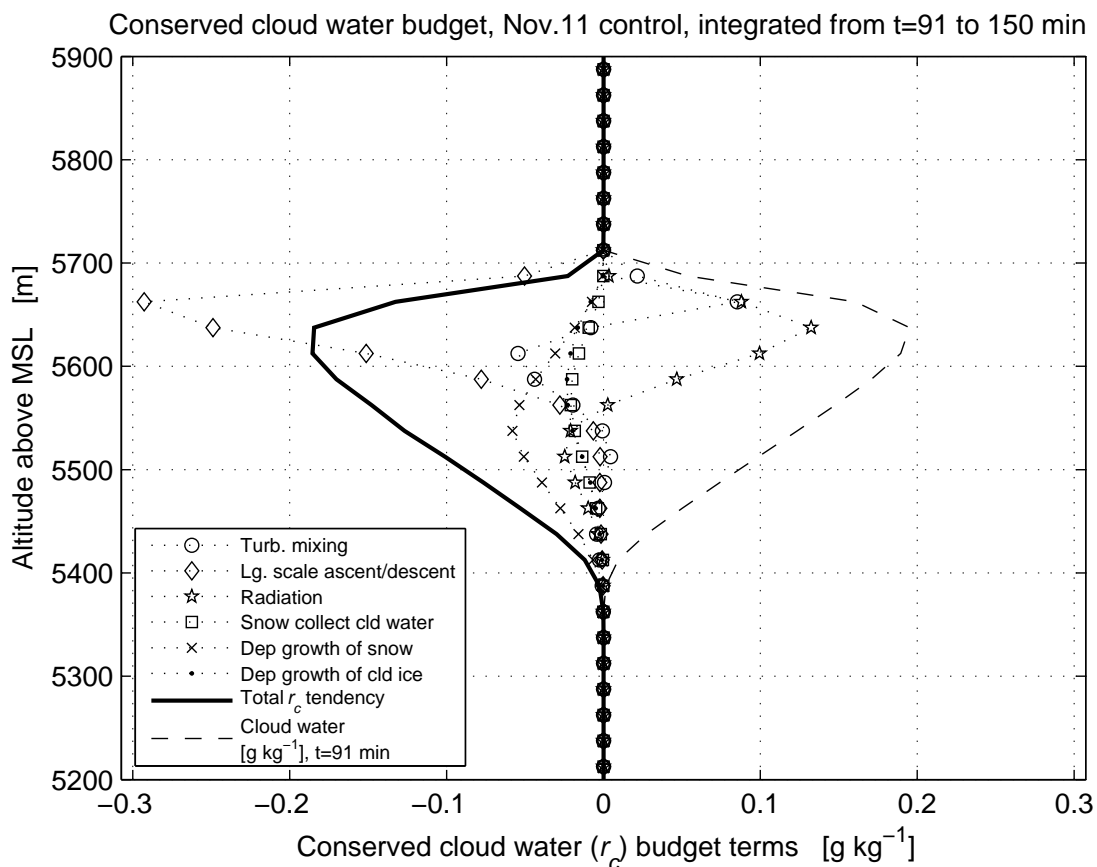


Figure 4.1: A budget of cloud water mixing ratio, r_c , for the Nov.11 control simulation. The budget is integrated over a one-hour period from $t = 91$ min to $t = 150$ min. The solid line indicates the overall change in r_c during the observed period. Symbols represent the effect on r_c due to individual model processes. Positive values indicate a source of liquid water, while negative values indicate a sink of liquid water.

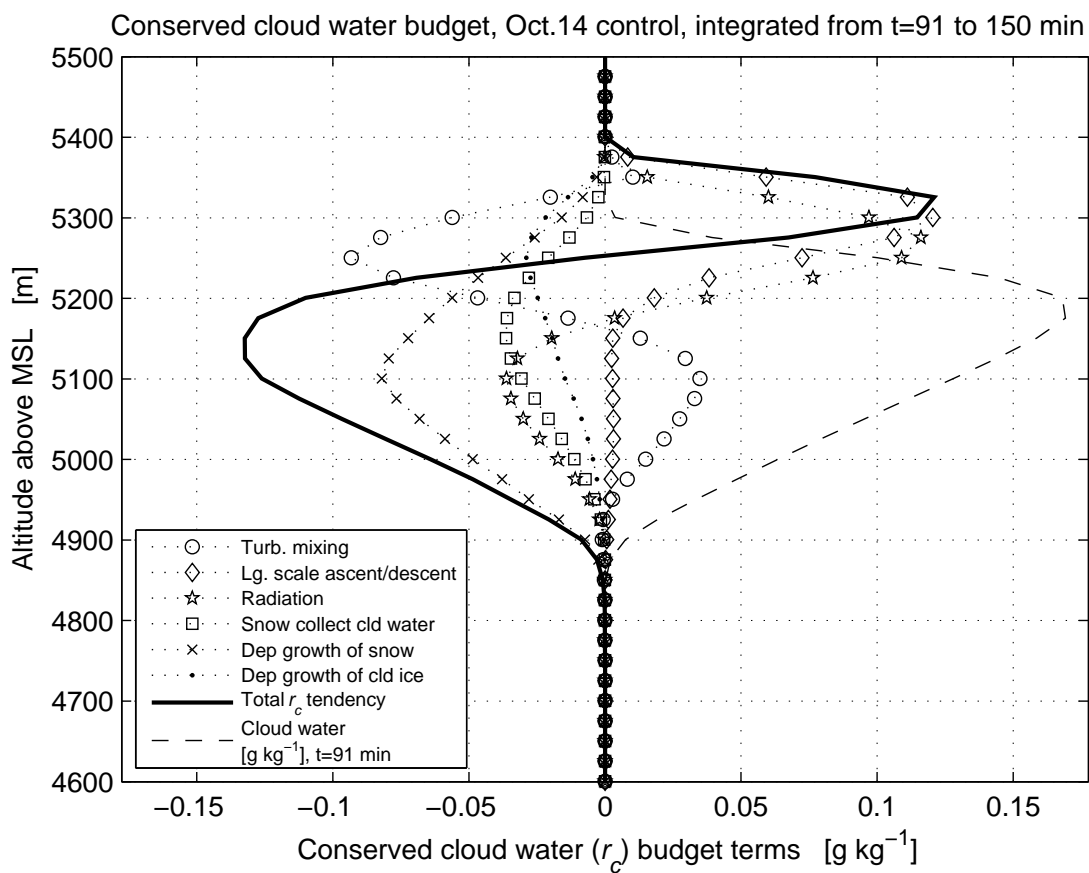


Figure 4.2: Same as figure 4.1, but for the Oct.14 control simulation.

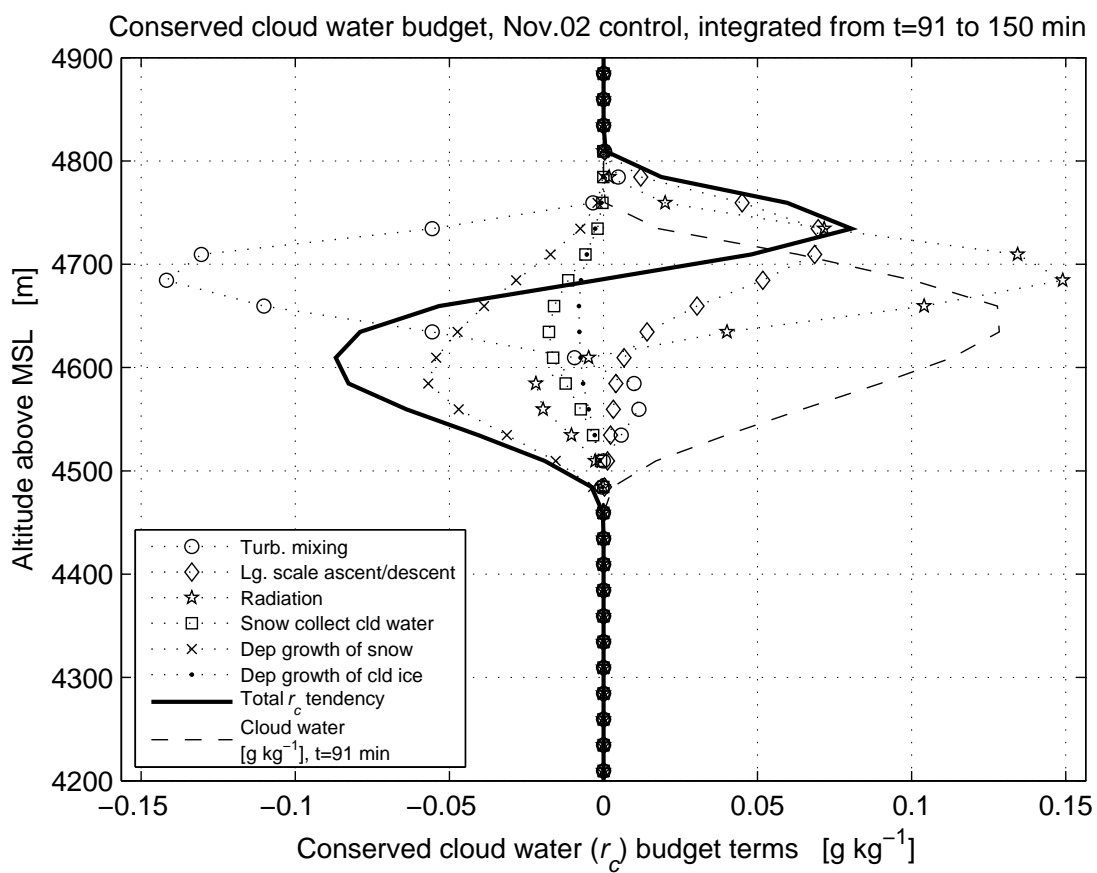


Figure 4.3: Same as figure 4.1, but for the Nov.02 control simulation.

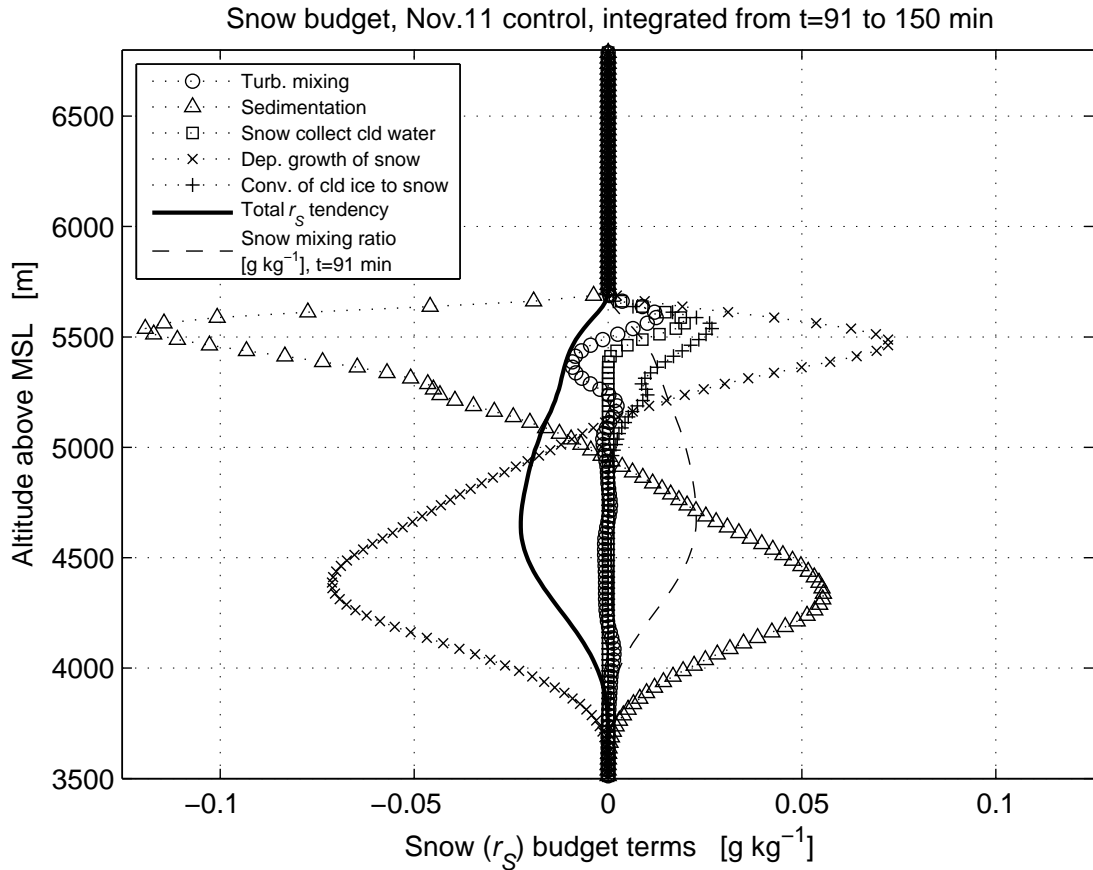


Figure 4.4: A budget of snow mixing ratio, r_S , for the Nov.11 control simulation. The budget is integrated over a one-hour period from $t = 91$ min to $t = 150$ min. The solid line indicates the overall change in r_S during the observed period. Symbols represent the effect on r_S due to individual model processes. Positive values indicate a source of snow mixing ratio, while negative values indicate a sink of snow mixing ratio. Processes such as large-scale ascent and radiation do not have a direct effect on snow in our simulations. Therefore, these terms are not included in the snow budget.

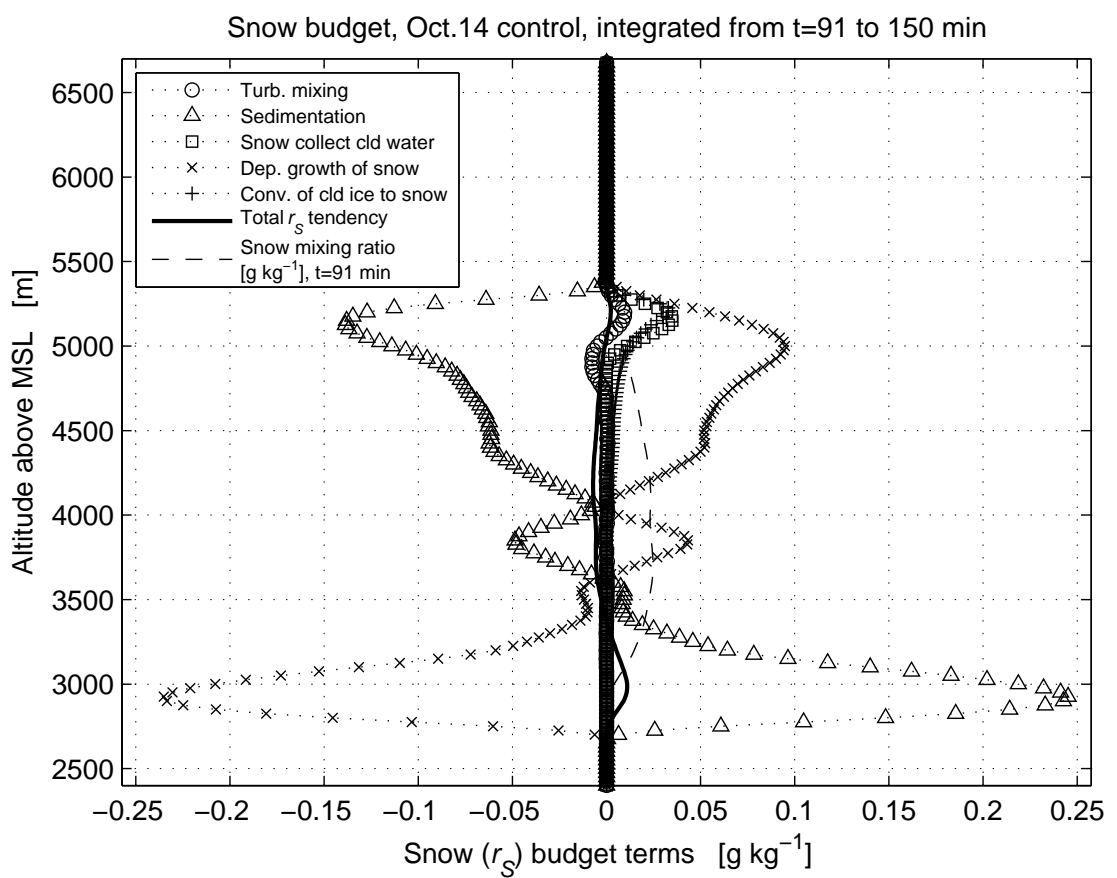


Figure 4.5: Same as figure 4.4, but for the Oct.14 control simulation.

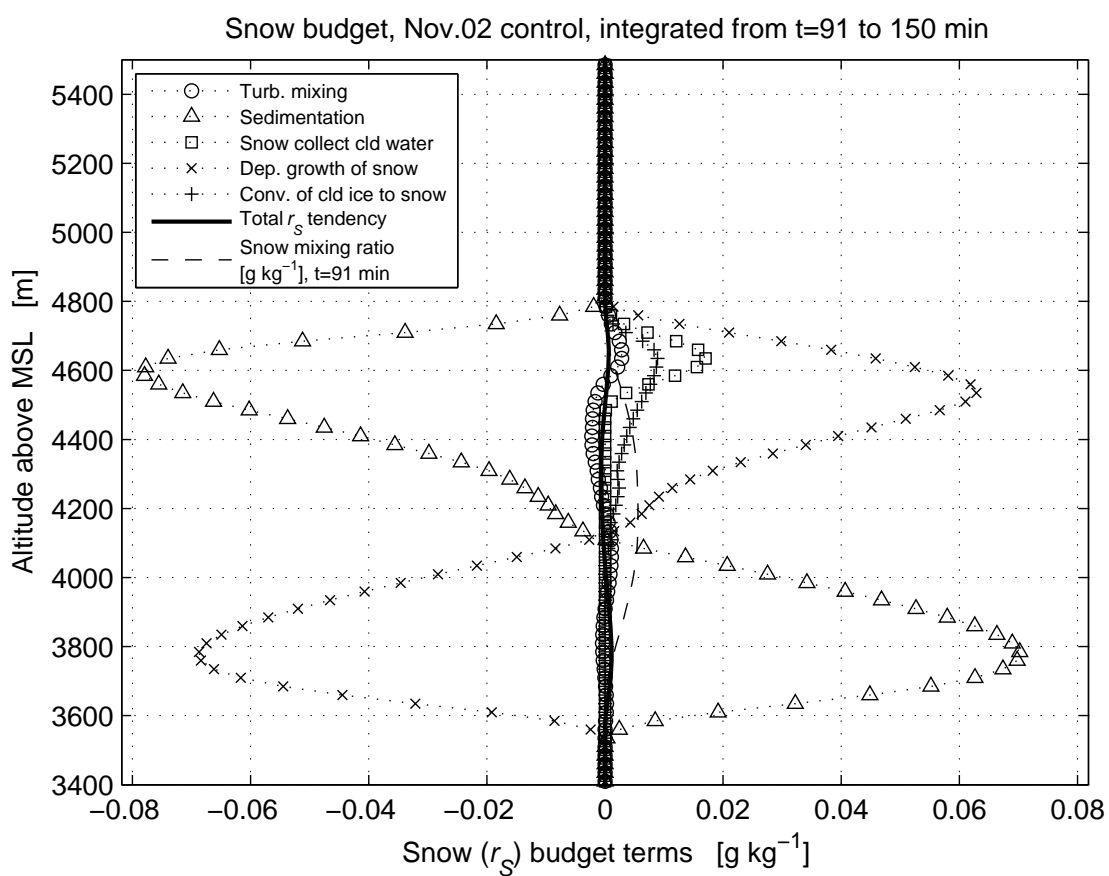


Figure 4.6: Same as figure 4.4, but for the Nov.02 control simulation.

Chapter 5

The development of analytic formulas for predicting snow mixing ratio and snow precipitation flux

To further understand snow formation within a mixed-phase cloud, we now create a series of analytic formulas. These equations predict the nature of snow particles without requiring a large amount of information. In the end, we hope to determine the amount of snow that falls from the base of a mixed-phase cloud.

In order to simplify our equations, we ignore processes that are shown in our graphical snow budgets (figures 4.4-4.6) to be small. Therefore, accretion and other small microphysical terms are not included in our equations. By ignoring some microphysical processes, our formulas cannot be completely accurate for all cases. However, the formula still provides a reasonable amount of information that can be analyzed in an informative manner.

NOTE: For a list of symbols used in this derivation, please refer to table 5.1.

To begin, we construct an equation for the depositional growth of snow mixing ratio, r_S :

$$\frac{\partial r_S}{\partial t} = -\frac{\partial(\overline{w_S r_S})}{\partial z} + \frac{\text{PSDEP}}{\rho}. \quad (5.1)$$

The term on the left-hand side represents the time tendency of snow mixing ratio, and the first term on the right-hand side represents the sedimentation of snow. The second term on the right hand side represents the increase in snow mixing ratio due to depositional growth.

We also allow for an power-law mass-diameter relationship by following Rutledge

and Hobbs (1983):

$$M_S = \alpha D_0^3 \frac{\pi}{6} \rho_S \left(\frac{D_S}{D_0} \right)^\beta. \quad (5.2)$$

The constant D_0 has units of length and is inserted in order to make the dimensions explicit. By modifying the constants α and β , the mass diameter relationship can be applied to snow habits. For our study, we select the Rutledge and Hobbs (1983) values of $\alpha = 1$ and $\beta = 3$, which correspond with spherical ice particles.

In order to generate an analytic equation from (5.1), we must explicitly define the individual terms. The snow fallspeed is given by Rutledge and Hobbs (1983) (A4):

$$w_S = a'' D_S^b \left(\frac{p_0}{p} \right)^{0.4}, \quad (5.3)$$

and the snow size distribution is given by Rutledge and Hobbs (1983) (2):

$$N_S = N_{0S} \exp(-\lambda_S D_S) dD_S. \quad (5.4)$$

By integrating (5.4), solving for D_S , and substituting the result into (5.3), we obtain the snow fallspeed averaged over a mass-weighted size distribution:

$$\overline{w_S} = a'' \left(\frac{p_0}{p} \right)^{0.4} \frac{1}{\lambda_S^b} \frac{\Gamma(\beta + b + 1)}{\Gamma(\beta + 1)}. \quad (5.5)$$

This formula matches Rutledge and Hobbs (1983) (A5) when $\beta = 3$.

It is preferable to replace λ_S in favor of r_S , since r_S is simpler to estimate. To do so, we relate r_S to the underlying exponential size distribution:

$$r_S = \frac{1}{\rho} \int_0^\infty N_{0S} \exp(-\lambda_S D_S) M_S dD_S. \quad (5.6)$$

Substituting in the mass-diameter relationship (5.2), we find:

$$\lambda_S = \left(\frac{\pi \rho_S \Gamma(\beta + 1) N_{0S}}{\rho} \frac{1}{6} \frac{1}{r_S} \alpha D_0^{3-\beta} \right)^{1/(\beta+1)}, \quad (5.7)$$

which reduces to Rutledge and Hobbs (1983) (3b) if $\alpha = 1$ and $\beta = 3$.

By substituting (5.7) for λ_S into (5.5), we find

$$\overline{w}_S = c_2 N_{0S}^{-b/(\beta+1)} r_S^{b/(\beta+1)}, \quad (5.8)$$

where

$$c_2 = a'' \left(\frac{p_0}{p} \right)^{0.4} \frac{\Gamma(\beta + b + 1)}{\Gamma(\beta + 1)} \left(\frac{\pi \rho_S \Gamma(\beta + 1)}{\rho} \frac{1}{6} \alpha D_0^{3-\beta} \right)^{-b/(\beta+1)}. \quad (5.9)$$

We now wish to obtain a substitution for the depositional growth rate of snow, *PSDEP*. The term originates from Rutledge and Hobbs (1983) (A16):

$$\frac{dM_S}{dt} = \frac{4\pi C(S_i - 1)}{A'' + B''}. \quad (5.10)$$

Here, the capacitance C of snow is required. In our study, we take the capacitance to be:

$$C = \frac{\gamma}{\pi} \left(\frac{D_S}{D_0} \right)^\nu, \quad (5.11)$$

where γ has units of length. When γ , ν , and D_0 all equal 1, then the formula becomes equivalent to Rutledge and Hobbs (1983) (A16).

By substituting (5.11) into (5.10), integrating over the size distribution (5.4), and multiplying by a constant ventilation factor of $F' = 2.7$, we find:

$$\begin{aligned} \frac{\text{PSDEP}}{\rho} &= \frac{1}{\rho} \frac{4\gamma(S_i - 1)N_{0S}}{A'' + B''} 2.7 \left(\frac{1}{D_0 \lambda_S} \right)^\nu \frac{1}{\lambda_S} \Gamma(\nu + 1) \\ &= c'_1 N_{0S} \lambda_S^{-\nu-1}, \end{aligned} \quad (5.12)$$

where

$$c'_1 = \frac{1}{\rho} \frac{4\gamma(S_i - 1)}{A'' + B''} 2.7 \left(\frac{1}{D_0} \right)^\nu \Gamma(\nu + 1), \quad (5.13)$$

$$A'' = \frac{L_v}{K_a T} \left(\frac{L_v}{R_v T} - 1 \right), \quad (5.14)$$

and

$$B'' = \frac{R_v T}{\chi e_{si}}. \quad (5.15)$$

(5.12) is similar to Rutledge and Hobbs (1983) (A26), except we use a single ventilation constant to substitute for a more complicated formula. Comparisons between (5.12) and Rutledge and Hobbs (1983) (A26) show that our selected value of $F' = 2.7$ is a good approximation for the ventilation constant (not shown).

If we now substitute the expression for λ_S (5.7) into (5.12), we obtain the following expression:

$$\frac{\text{PSDEP}}{\rho} = c'_3 N_{0S}^{\left(\frac{\beta-\nu}{\beta+1}\right)} r_S^{\left(\frac{\nu+1}{\beta+1}\right)}. \quad (5.16)$$

where

$$c'_3 = c'_1 \left(\frac{\pi \rho_S \Gamma(\beta + 1)}{\rho} \frac{\alpha D_0^{3-\beta}}{6} \right)^{(-\nu-1)/(\beta+1)}. \quad (5.17)$$

We now return to our original snow budget, which is defined by (5.1). To simplify our final equations, we assume the Bousinesq approximation in order to disregard gradients of density in the vertical. We also note our previous observation that sedimentation and depositional growth of snow have a net effect on snow of nearly zero in two of our cloud cases. Therefore, we assume that $\frac{\partial r_S}{\partial t} = 0$. By doing so, our analytic snow budget becomes:

$$\frac{d(-\overline{w_S} r_S)}{dz} = \frac{\text{PSDEP}}{\rho}. \quad (5.18)$$

The minus sign arises because w_S is defined as a positive quantity even though snow falls downward.

It is important to note that in reality, precipitation flux cannot be represented by a strictly steady-state equation. However, our goal is to approximate the amount of precipitation at a specific instant. Therefore, it is acceptable to assume a steady-state equation for our study.

We now substitute (5.8) for w_S . After taking the derivative, the left-hand side of (5.18) becomes:

$$\frac{d(-\overline{w_S r_S})}{dz} = -c_2 \left(1 + \frac{b}{\beta + 1} \right) N_{0S}^{-b/(\beta+1)} r_S^{b/(\beta+1)} \frac{dr_S}{dz}. \quad (5.19)$$

After substituting (5.16) into the right-hand side and integrating, we can solve (5.18) for r_S to obtain:

$$r_S = \left[\frac{c'_3}{c_2} \frac{\beta + b - \nu}{\beta + b + 1} N_{0S}^{\frac{b+\beta-\nu}{\beta+1}} (z_{top} - z) + r_{S,top}^{\frac{\beta+b-\nu}{\beta+1}} \right]^{\frac{\beta+1}{b-\nu+\beta}}, \quad (5.20)$$

or, if r_S at the top is zero,

$$r_S = N_{0S} \left[\frac{c'_3}{c_2} \frac{\beta + b - \nu}{\beta + b + 1} (z_{top} - z) \right]^{\frac{\beta+1}{b-\nu+\beta}}. \quad (5.21)$$

For reference, we can define w_s in terms of external quantities by substituting (5.21) into (5.8):

$$w_S = c_2^{\frac{-\nu+\beta}{b-\nu+\beta}} \left[c'_3 \frac{\beta + b - \nu}{\beta + b + 1} (z_{top} - z) \right]^{\frac{b}{b-\nu+\beta}}. \quad (5.22)$$

Finally, by multiplying (5.21) by (5.8), we obtain the final equation for estimating snow precipitation falling from a desired altitude:

$$F_{PSDEP} = \overline{w_S r_S} = N_{0S} c_2^{\frac{-\nu-1}{b-\nu+\beta}} \left[c'_3 \frac{\beta + b - \nu}{\beta + b + 1} (z_{top} - z) \right]^{\frac{\beta+b+1}{b-\nu+\beta}}. \quad (5.23)$$

The end result of this derivation is a pair of analytic formulas that calculate snow properties. Equation (5.21) approximates mixing ratio at the base of a mixed-phase

layer, while equation (5.23) approximates the flux of snow falling through the base of the layer. An equation for diagnosing the average snow fall velocity (5.22) is also provided for reference, but it is not verified in this study.

Each of these analytic equations depends on a limited set of factors: temperature (T), air density (ρ), pressure (p), mixed-phase layer thickness ($z_{top} - z$), amount of saturation (S_i), and saturation vapor pressure (e_{si}). If we select values for these parameters that represent the base of a mixed-phase layer, we can approximate snow properties without using remote sensing equipment or detailed aircraft data. While our formulas are not a substitute for these types of data, we can still calculate first-guess conditions to determine whether a mixed-phase cloud will glaciate, or whether it will remain a mixed-phase cloud. We analyze the accuracy of our formulas in chapter 6.

Table 5.1: A list of symbols used to derive diagnostic equations (5.20) and (5.23). Units and values correspond to those used in our control simulations.

Symbol	Description	Value	Units
A''	Thermodynamic term		m s kg^{-1}
a''	Constant in snow fallspeed relationship	2.35	$\text{m}^{1-b} \text{s}^{-1}$
B''	Thermodynamic term		m s kg^{-1}
b	Fallspeed exponent for snow	0.11	
C	Capacitance of snow		m
c'_1	Term for calculating c'_3		$\text{m}^2 \text{s}^{-1}$
c_2	Term for calculating w_s		$\text{m}^{1-b} \text{s}^{-1}$
c'_3	Term for calculating $\frac{PSDEP}{\rho}$		$\text{m}^2 \text{s}^{-1}$
D_0	Unit length	1	m
D_S	Diameter of snow		m
$\overline{D_S}$	Horiz. averaged diameter of snow		m
e_{si}	Saturation vapor pressure for ice		N m^{-2}
F'	Approximated ventilation factor	2.7	
F_{PSDEP}	Flux of falling snow		$\text{kg kg}^{-1} \text{m s}^{-1}$
K_a	Thermal conductivity of air	2.43e2	$\text{J m}^{-1} \text{s}^{-1} \text{K}^{-1}$
L_s	Latent heat of sublimation	2.5e6	J kg^{-1}
M_S	Mass of snow		kg
\overline{N}	Horiz. averaged snow number concentration		m^{-3}
N_S	Number concentration of snow		m^{-3}
N_{0S}	Intercept for snow size distribution	2e7*	m^{-4}
p	Pressure		N m^2
p_0	Reference pressure		N m^2
$PSDEP$	Rate of depositional growth of snow		$\text{kg m}^{-3} \text{s}^{-1}$
r_S	Snow mixing ratio		kg kg^{-1}
$r_{S,top}$	Snow mixing ratio at cloud top		kg kg^{-1}
R_v	Specific heat of water vapor	461.5	$\text{J kg}^{-1} \text{K}^{-1}$
S_i	Saturation ratio with respect to ice		$\text{kg m}^{-3} \text{s}^{-1}$
t	Time		s
w_S	Fallspeed of snow		m s^{-1}
$\overline{w_S}$	Mass-weighted fallspeed of snow		m s^{-1}
z	Altitude		m
z_{top}	Altitude at cloud top		m
α	Dimensionless constant	1	
β	Dimensionless constant	3	
χ	Diffusivity of water vapor in air	2.26e-5	$\text{m}^2 \text{s}^{-1}$
Γ	Gamma function		
γ	Constant in equation for snow capacitance	1	m
ν	Exponent in equation for snow capacitance	1	
ρ	Density of air		kg m^{-3}
ρ_S	Density of snow	100.0	kg m^{-3}
λ_S	Slope of snow size distribution		m^{-1}

Chapter 6

Verification of the snow mixing ratio and snow precipitation flux formulas

In order to verify the accuracy of our approximations, we must test them over a wide range of conditions. To do so, we generate a sensitivity study by varying conditions that modify the amount of snow produced. These conditions are a'' , which affects the fall velocity of snow; N_{0S} , which affects the number of snow particles produced; and large-scale ascent (V_{ls}), which modifies the underlying saturation of the cloud. Specific settings for each variable are described in tables 6.1 and 6.2.

For each cloud case, we select a single sensitivity parameter and select an appropriate setting from table 6.1 or table 6.2. All other sensitivity parameters are set to their control values, and the simulation is re-run. We then calculate the approximated snow mixing ratio using (5.20) and compare the result to the simulated mixing ratio from each simulation. We also calculate the amount of snow precipitation flux using (5.23), and compare it to the “actual” value obtained from the simulation.

The observation time selected for each sensitivity simulation will vary. We choose the observation time based on when the maximum magnitude of snow mixing ratio occurs in each sensitivity simulation. This is done in order to minimize the total time tendency that occurs during observation. The less time tendency that is present, the fewer errors will appear in our analytic formula.

Because our analytic formulas do not include collection, we deactivate collection processes in our sensitivity simulations. This allows us to determine the relative accuracy of our analytic formula using similar simulated conditions. A future study

could compare the accuracy of the equations once collection is re-introduced into the simulations.

Results from our comparison are shown in figures 6.1 and 6.2. Each point represents a single simulation, with the vertical position denoting the amount of actual precipitation flux from our model, and the horizontal position denoting the amount of precipitation flux calculated by our formula. Symbols denote the cloud case and the sensitivity parameter being varied. The solid line denotes where diagnosed values are equal to the simulated values. Points to the left of the line indicate that our formula is underestimating precipitation flux, while points to the right of the line indicate our formula is overestimating precipitation flux.

We find that formulas (5.21) and (5.23) consistently underpredict snow mixing ratio and precipitation flux for most cases. The exact amount of underprediction varies with each simulation, and there is no apparent trend with regard to the adjusted sensitivity parameter. A few cases do produce an analytic prediction that is approximately equal to the simulated results, but there is no noticeable correlation between these simulations.

The underprediction trend can be explained in several ways. First, in (5.18), we disregard the time tendency of the snow mixing ratio. While this assumption allows for a simplified formula, our graphical budgets indicate the time tendency is small but non-zero for our control cases. Therefore, including the time tendency in our equations could improve prediction of both mixing ratio and precipitation flux. However, adding the time tendency severely complicates our budget equation, and could produce an equation that is not explicitly solvable. A useful future study could attempt to re-derive the equations while including the time tendency of snow.

Because depositional growth of snow and sedimentation are predominant processes affecting our simulated mixed-phase clouds, our equations focus on these two terms. However, we do neglect the other processes presented in our graphical bud-

gets, including turbulent mixing and conversion of cloud ice to snow. These terms are non-zero at cloud base, so neglecting these processes will also produce errors in our results.

However, we do find that our formulas produce relatively precise estimations of precipitation flux. It is possible that a multiplicative or additive constant could be applied to our results to compensate for errors. A properly calculated constant would account for the processes not included in our formulas, such as time tendency and collection by snow. However, we leave the calculation of a constant to a future study.

Table 6.1: Imposed sensitivity values of large-scale vertical velocity (V_{ls}) for each cloud case. Positive values indicate ascent. In each sensitivity study, a single value of ascent or descent is selected. All other parameters are set to their control values. An asterisk denotes the control setting for each cloud case.

Cloud case	Imposed vertical velocity settings				
Nov.11	-5 cm s ⁻¹	-3 cm s ⁻¹ *	-1 cm s ⁻¹	1 cm s ⁻¹	3 cm s ⁻¹
Oct.14	-4 cm s ⁻¹	-2 cm s ⁻¹	0 cm s ⁻¹	1.4 cm s ⁻¹ *	4 cm s ⁻¹
Nov.02	-3 cm s ⁻¹	-1 cm s ⁻¹	0.7 cm s ⁻¹ *	3 cm s ⁻¹	5 cm s ⁻¹

Table 6.2: Imposed sensitivity values of a'' and N_{0S} . Only one variable is modified for each of these sensitivity cases, while the other variable is set to the control value. An asterisk denotes the control setting for each cloud case.

Variable	Units	Imposed variable settings						
a''	m ^{1-b} s ⁻¹	0.29375	0.5875	1.175	2.35*	4.70	9.40	18.80
N_{0S}	m ⁻⁴	2.5e6	5.0e6	1.0e7	2.0e7*	4.0e7	8.0e7	1.60e8

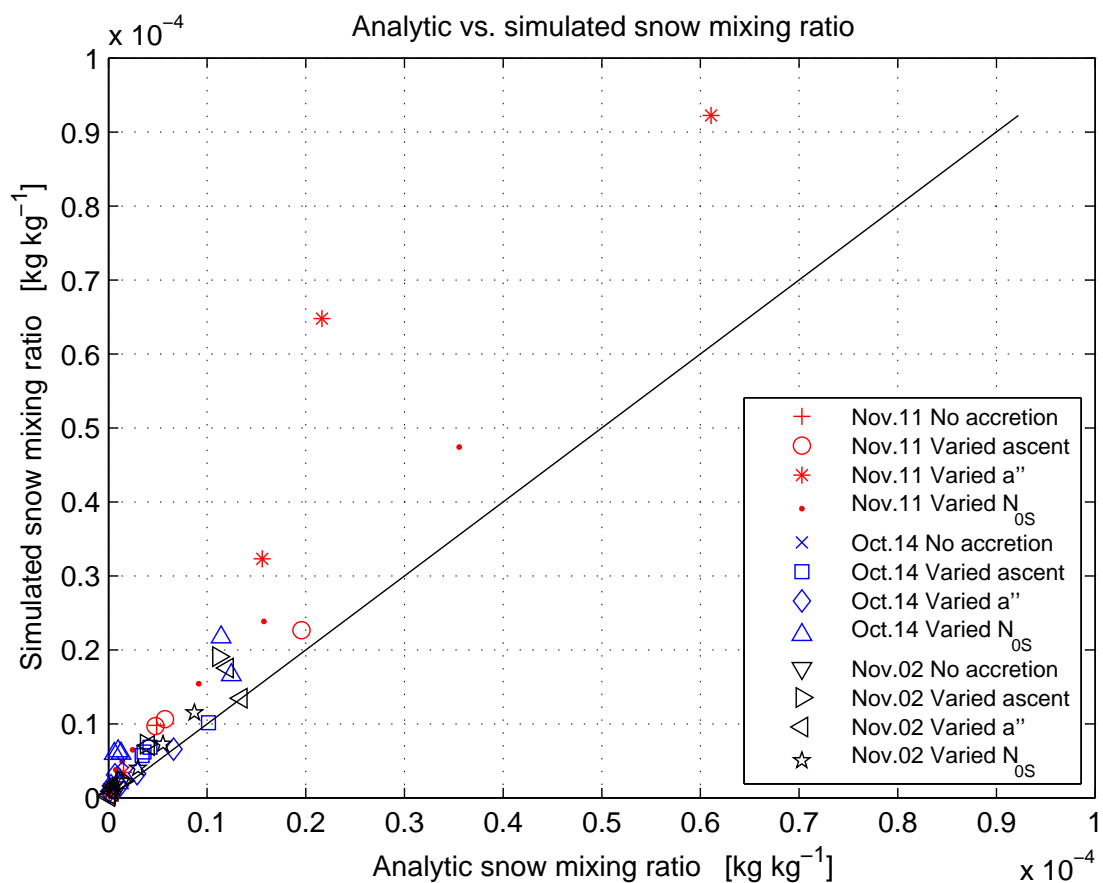


Figure 6.1: A scatter plot comparing calculated results from the right-hand side of ((5.20), x-axis) versus the left-hand side obtained directly from the COAMPS-LES sensitivity simulations (y-axis). The solid line indicates equality between the compared values. Points to the left of the line show that our formula underestimates snow precipitation flux, while points to the right of the line show our formula overestimates snow precipitation flux. Symbols denote the cloud case being observed and which sensitivity parameter is being varied.

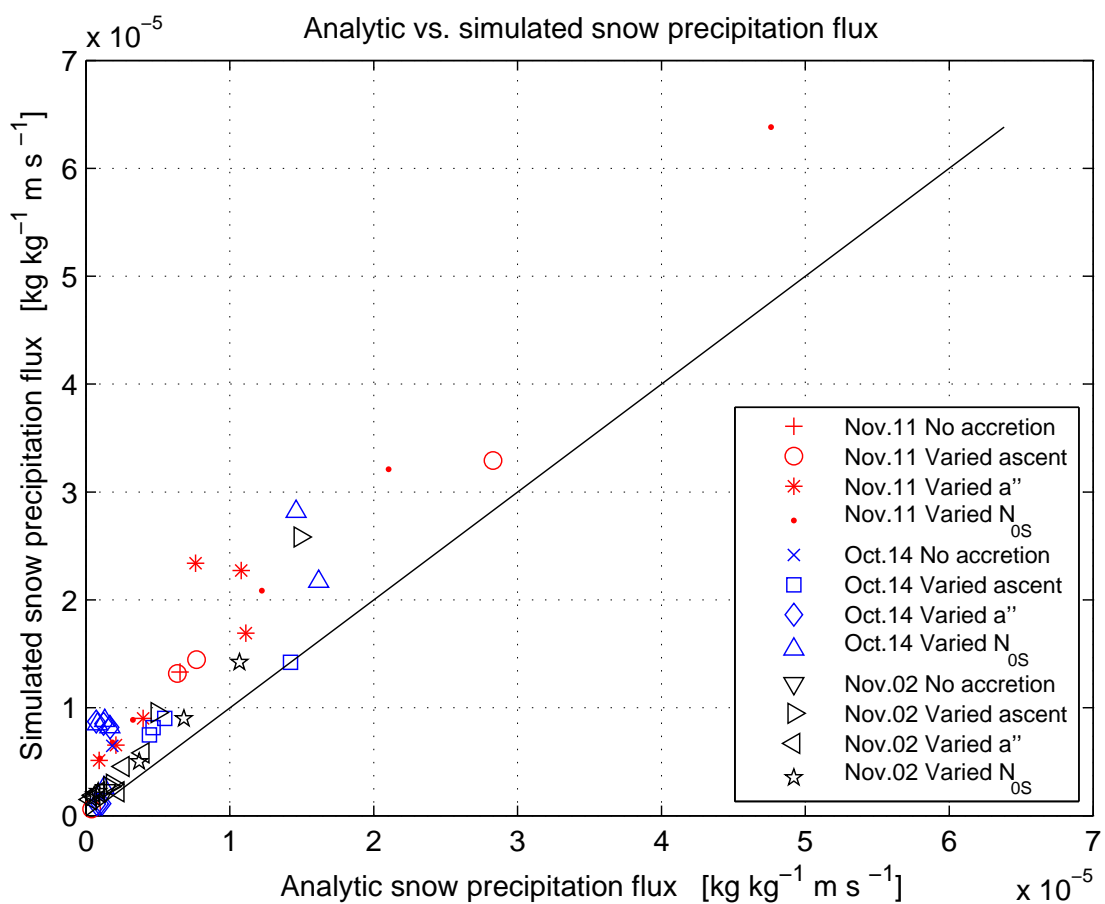


Figure 6.2: Same as figure (6.1), but comparing calculated snow precipitation flux from (5.23, x-axis) versus simulated snow precipitation flux (y-axis).

Chapter 7

Conclusions

In this study, we perform a series of high-resolution three-dimensional simulation to examine three mixed-phase alto clouds. Each cloud was observed by aircraft, allowing our study to focus on realistic atmospheric conditions. Each simulation is analyzed in order to investigate the tendencies of the liquid and ice water within the clouds. The goal of our study is to determine which microphysical processes contribute to snow formation within a mixed-phase cloud.

We first present a budget equation analyzing changes in liquid water (equation (4.1)). Using this budget, we can graphically determine which model processes have the largest effect on depleting or enhancing liquid water mixing ratio (figures 4.1-4.3). The results show that depositional growth of snow is the predominant microphysical process leading to liquid depletion in all cloud cases. Other microphysical terms also provide a less significant contribution to the depletion of liquid water.

Next, a budget equation for snow (4.2) is examined. This budget determines which model processes lead to the greatest modification of snow mixing ratio (figures 4.4-4.6). We find that in all three simulated cloud cases, depositional growth is the primary mechanism for enhancing snow mixing ratio within cloud. Below cloud, sublimation also acts as a primary method of removing snow. Other microphysical processes provide a relatively small contribution to snow enhancement. Sedimentation, or the motion of falling snow, acts as a balancing factor to the depositional growth. Thus, we find that processes of sedimentation and depositional growth (loss) produce a net effect of nearly zero in two cloud cases.

Finally, we create a series of analytic equations to approximate snow behavior

at the base of a mixed-phase cloud. These formulas are calculated based on methods from Rutledge and Hobbs (1983). The primary presumption is that the main source of snow growth in a mixed-phase layer is depositional growth, and the main source of depletion is sedimentation. We also presume that these two processes are nearly balanced, and the tendency of snow mixing ratio does not change with time. The resulting equations, (5.21) and (5.23), predict the snow mixing ratio and snow precipitation flux of at the base of a cloud. These equations do not require the knowledge of detailed in-cloud conditions. Instead, they approximate snow behavior based on reasonable values of temperature, pressure, and other simple variables.

To verify the formulas are accurate for a wide variety of conditions, we perform a series of sensitivity simulations, and then calculate the diagnosed snow mixing ratio and precipitation flux for each simulation. We compare the diagnosed results with the simulations in figures 6.1 and 6.2. We find that our current analytic formulas tend to underpredict snow mixing ratio and precipitation flux, regardless of the varied conditions. However, our formulas do provide a reasonable first-guess prediction of cloud conditions.

We find that with a single-moment bulk microphysics scheme, we can produce reasonable estimates of cloud behavior. However, more complicated microphysics schemes may provide improved methods for simulating microphysical phase. Further study could involve comparing our results versus a more complicated microphysics scheme. These comparisons could provide insight into how our formulas can be improved.

BIBLIOGRAPHY

- Ackerman, T. P. and Co-Authors, 2004: Atmospheric Radiation Measurement program science plan. <http://www.arm.gov/science>.
- Cober, S. G. and G. A. Isaac, 2002: Aircraft icing environments observed in mixed-phase clouds. Preprints, *40th Aerospace Sciences Meeting & Exhibit*, Reno, NV, American Institute of Aeronautics and Astronautics.
- Cooper, W. A., 1986: Ice initiation in natural clouds. *Precipitation Enhancement - A Scientific Challenge*, Meteor. Monogr., No. 43, Amer. Meteor. Soc., 29–32.
- Duynkerke, P. G. and Co-Authors, 2004: Observations and numerical simulations of the diurnal cycle of the EUROCS stratocumulus case. *Quart. J. Roy. Meteor. Soc.*, **130**, 3269–3296.
- Falk, M. J. and V. E. Larson, 2007: What causes partial cloudiness to form in multilayered midlevel clouds? A simulated case study. *J. Geophys. Res.*, **112** (D12206), doi:10.1029/2006JD007666.
- Ferrier, B. S., 1994: A double-moment multiple-phase four-class bulk ice scheme. Part I: Description. *J. Atm. Sci.*, **51**, 249–280.
- Fleishauer, R. P., V. E. Larson, and T. H. Vonder Haar, 2002: Observed microphysical structure of midlevel, mixed-phase clouds. *J. Atmos. Sci.*, **59**, 1779–1804.
- Fletcher, N. H., 1962: *The Physics of Rainclouds*. Cambridge University Press, 386 pp.

- Fowler, L. D., D. A. Randall, and S. A. Rutledge, 1996: Liquid and ice cloud microphysics in the CSU general circulation model. Part I: Model description and simulated microphysical processes. *J. Climate*, **9**, 489–529.
- Golaz, J.-C., S. Wang, J. D. Doyle, and J. M. Schmidt, 2005: Second and third moment vertical velocity budgets derived from COAMPS-LES. *Bound.-Layer Meteor.*, **116**, 487–517.
- Haulman, D. L., 2003: U.S. unmanned aerial vehicles in combat, 1991-2003. Report, Air Force Historical Research Agency, 19 pp., Maxwell AFB, AL.
- Hodur, R. M., 1997: The Naval Research Laboratory's Coupled Ocean/Atmosphere Mesoscale Prediction System (COAMPS). *Mon. Wea. Rev.*, **125**, 1414–1430.
- Kankiewicz, J. A., L. D. Carey, J. M. Davis, J. M. Forsythe, D. L. Reinke, and T. H. Vonder Haar, 2006: The morphology of two mixed phase clouds. Preprints, *11th Conf. on Cloud Physics*, Ogden, UT, Amer. Meteor. Soc.
- Larson, V. E., K. E. Kotenberg, and N. B. Wood, 2007: An analytic longwave radiation formula for liquid layer clouds. *Mon. Wea. Rev.*, **135**, 689–699.
- Larson, V. E., A. J. Smith, M. J. Falk, K. E. Kotenberg, and J.-C. Golaz, 2006: What determines altocumulus dissipation time? *J. Geophys. Res.*, **111** (D19207), doi:10.1029/2005JD007002.
- Liou, K. N., 2002: *An Introduction to Atmospheric Radiation*. 2d ed., Academic Press, 583 pp.
- Long, M. L., 2003: COAMPSTM Version 3 Model Description - General Theory and Equations. NRL Publication NRL/PU/7500-03-448, Technical Information Services Branch, Naval Research Laboratory, 143 pp., Washington, DC.

- Lynn, B. H., A. P. Khain, J. Dudhia, D. Rosenfeld, A. Pokrovsky, and A. Seifert, 2005: Spectral (bin) microphysics coupled with a mesoscale model (MM5). Part I: Model description and first results. *Mon. Wea. Rev.*, **133**, 44–58.
- Meyers, M. P., P. J. D. Mott, and W. R. Cotton, 1992: New primary ice-nucleation parameterizations in an explicit cloud model. *J. Appl. Meteor.*, **31**, 708–721.
- Morrison, H., J. A. Curry, and V. I. Khvorostyanov, 2005: A new double-moment microphysics parameterization for application in cloud and climate models. Part I: Description. *J. Atmos. Sci.*, **62**, 1665–1677.
- Niu, J., L. D. Carey, P. Yang, J. A. Kankiewicz, and T. H. Vonder Haar, 2006: A common microphysical structure for midlevel mixed phase clouds in the mid-latitudes: Results from the Cloud Layer Experiment (CLEX-9). Preprints, *Twelfth Conference on Cloud Physics*, Madison, WI, Amer. Meteor. Soc.
- Reisin, T., Z. Levin, and S. Tzivion, 1996: Rain production in convective clouds as simulated in an axisymmetric model with detailed microphysics. Part I: Description of the model. *J. Atmos. Sci.*, **53**, 497–519.
- Rutledge, S. A. and P. V. Hobbs, 1983: The mesoscale and microscale structure of organization of clouds and precipitation in midlatitude cyclones. VIII: A model for the “seeder-feeder” process in warm-frontal rainbands. *J. Atmos. Sci.*, **40**, 1185–1206.
- Sassen, K. and V. I. Khvorostyanov, 2007: Microphysical and radiative properties of mixed-phase altocumulus: A model evaluation of glaciation effects. *Atm. Res.*, **84**, 390–398.
- Shettle, E. P. and J. A. Weinman, 1970: The transfer of solar irradiance through inhomogeneous turbid atmospheres evaluated by Eddington’s approximation. *J. Atmos. Sci.*, **27**, 1048–1055.

- Stevens, B. and Co-Authors, 2005: Evaluation of large-eddy simulations via observations of nocturnal marine stratocumulus. *Mon. Wea. Rev.*, **133**, 1443–1462.
- Stull, R. B., 1988: *An Introduction to Boundary Layer Meteorology*. Kluwer Academic Publishers, 666 pp.
- Vonder Haar, T. H. and Co-Authors, 1997: Overview and objectives of the DoD Center for Geosciences sponsored “Complex Layered-Cloud Experiment”. Preprints, *Cloud Impacts on DoD Operations and Systems Conf.*, Newport, RI, Phillips Laboratories, 163–169.
- Warren, S. G., C. J. Hahn, J. London, R. M. Chervin, and R. Jenne, 1988a: Global distribution of total cloud cover and cloud type amount over land. *Tech. Report NCAR TN-317 STR*, Natl. Cent. for Atmos. Res., Boulder, CO.
- Warren, S. G., C. J. Hahn, J. London, R. M. Chervin, and R. Jenne, 1988b: Global distribution of total cloud cover and cloud type amount over the ocean. *Tech. Report NCAR TN-317 STR*, Natl. Cent. for Atmos. Res., Boulder, CO.
- Zhang, M. H. and Co-Authors, 2005: Comparing clouds and their seasonal variations in 10 atmospheric general circulation models with satellite measurements. *J. Geophys. Res.*, **110** (D15S02), doi:10.1029/2004JD005021.